



ELSEVIER

Deep-Sea Research II 51 (2004) 3069–3101

DEEP-SEA RESEARCH
PART II

www.elsevier.com/locate/dsr2

The accuracy of surface elevations in forward global barotropic and baroclinic tide models

Brian K. Arbic^{a,*}, Stephen T. Garner^b, Robert W. Hallberg^b,
Harper L. Simmons^{b,c}

^a*Program in Atmospheric and Oceanic Sciences, Princeton University, P.O. Box CN710, Sayre Hall, Princeton, NJ 08544-0710, USA*

^b*Geophysical Fluid Dynamics Laboratory/NOAA, Princeton, NJ 08542, USA*

^c*International Arctic Research Center, University of Alaska Fairbanks, Fairbanks, AK, 99775, USA*

Abstract

This paper examines the accuracy of surface elevations in a forward global numerical model of 10 tidal constituents. Both one-layer and two-layer simulations are performed. As far as the authors are aware, the two-layer simulations and the simulations in a companion paper (Deep-Sea Research II, 51 (2004) 3043) represent the first published global numerical solutions for baroclinic tides. Self-consistent forward solutions for the global tide are achieved with a convergent iteration procedure for the self-attraction and loading term. Energies are too large, and elevation accuracies are poor, unless substantial abyssal drag is present. Reasonably accurate tidal elevations can be obtained with a spatially uniform bulk drag c_d or horizontal viscosity K_H , but only if these are inordinately large. More plausible schemes concentrate drag over rough topography. The topographic drag scheme used here is based on an exact analytical solution for arbitrary small-amplitude terrain, and supplemented by dimensional analysis to account for drag due to flow-splitting and low-level turbulence as well as that due to breaking of radiating waves. The scheme is augmented by a multiplicative factor tuned to minimize elevation discrepancies with respect to the TOPEX/POSEIDON (T/P)-constrained GOT99.2 model. The multiplicative factor may account for undersampled small spatial scales in bathymetric datasets. An optimally tuned multi-constituent one-layer simulation has an RMS elevation discrepancy of 9.54 cm with respect to GOT99.2, in waters deeper than 1000 m and over latitudes covered by T/P (66°N to 66°S). The surface elevation discrepancy decreases to 8.90 cm (92 percent of the height variance captured) in the optimally tuned two-layer solution. The improvement in accuracy is not due to the direct surface elevation signature of internal tides, which is of small amplitude, but to a shift in the barotropic tide induced by baroclinicity. Elevations are also more accurate in the two-layer model when pelagic tide gauges are used as the benchmark, and when the T/P-constrained TPXO6.2 model is used as a benchmark in deep waters south of 66°S. For Antarctic diurnal tides, the improvement in forward model elevation accuracy with baroclinicity is substantial. The optimal multiplicative factor in the two-layer case is nearly the same as in the one-layer case, against initial expectations that the explicit resolution of

*Corresponding author.

E-mail address: arbic@splash.princeton.edu (B.K. Arbic).

low-mode conversion would allow less parameterized drag. In the optimally tuned two-layer M_2 solution, local values of the ratio of temporally averaged squared upper layer speed to squared lower layer speed often exceed 10.

© 2004 Elsevier Ltd. All rights reserved.

1. Introduction

Tides are the simplest large-scale motions in the open ocean. The barotropic tidal response in the mid-ocean is linear. Compared to the oceanic general circulation, tides are controlled by relatively few physical processes. In contrast to the wind- and buoyancy-forcing fields, tidal forcing has a spatial and temporal structure that is known very accurately. Yet it is only in the last few decades that open ocean tidal elevations have been mapped to high accuracy. Accurate charts have been constructed with models that are constrained by either tide-gauge or satellite altimetry data. The relative simplicity of tides makes the challenge of mapping them globally in forward models, that is, models that are unconstrained by data, an appealing one. Forward global tide models are an ideal testing ground for the hydrodynamical cores of numerical ocean general circulation models, and for ideas about drag and dissipation. In contrast to data-constrained models, forward models cannot achieve accurate tidal elevations unless substantial parameterized drag is included in the abyss. Forward models thus point clearly to drag in the open ocean as a central control on tidal flow. In agreement with other recent studies of global forward tide models (Jayne and St. Laurent, 2001—hereafter JS; Carrere and Lyard, 2003—hereafter CL; Egbert et al., 2004—hereafter ERB), we argue that topographic drag is a plausible mechanism for mid-ocean tidal dissipation. (Note that CL focused mostly on wind-driven motions and discussed tides only briefly.) Topographic drag probably affects all large-scale oceanic motions, and the understanding gained through use of forward tide models should be helpful in planning numerical simulations that simultaneously contain tides and the general circulation. This paper focuses on three factors—self-attraction and loading, topographic drag, and baroclinicity—that affect the accuracy of global forward

modeled tidal elevations. To the best of our knowledge, the two-layer simulations presented in the current paper and the simulations of Simmons, Hallberg, and Arbic (this issue; hereafter SHA) are the first published global simulations of baroclinic tides. There are several differences between SHA and the present study. In place of the full spherical harmonic computation of the self-attraction and loading term, SHA used the scalar approximation, which facilitated the performance of higher resolution simulations. SHA focused on the rate of energy conversion from barotropic to resolved low-mode baroclinic motions, rather than the accuracy of surface elevations, and SHA did not utilize a parameterization of topographic drag.

Both observational and theoretical work on tides have a long history (Cartwright, 1999). Much of the theoretical work has been done in idealized geometries. The development of modern computers led to numerical tidal models with realistic geometry and bathymetry. Hendershott (1977, 1981) and Schwiderski (1980) review the pioneering work. Early successes at constraining hydrodynamical tide models by tide-gauge data were achieved by Parke and Hendershott (1980) and Schwiderski (1980). A tide model was derived solely from Geosat altimetric data by Cartwright and Ray (1990). Both the Schwiderski and Cartwright and Ray models have a combined elevation accuracy over the eight largest tidal constituents of about 4.5 cm, relative to deep-ocean tide gauges (Shum et al., 1997). With the launch of the TOPEX/POSEIDON (T/P) altimeter in 1992, the need to subtract out tidal elevations, so that other oceanic motions could be studied, stimulated the development of over 20 data-constrained models. All agreed with deep-ocean tide gauges to order 2.5–3 cm (Andersen et al., 1995; Le Provost et al., 1995; Shum et al., 1997). Le Provost et al. (1994) ran a hydrodynamical model which utilized tide-gauge data, albeit in a somewhat subtle manner—

see ERB for a discussion. Since the Le Provost et al. model was independent of altimetric data, it served as an important check on other data-constrained models, which were either entirely derived from T/P data (e.g. Desai and Wahr, 1995) or assimilated T/P data into hydrodynamical cores (e.g. Egbert et al., 1994).

The total dissipation of tidal energy can be inferred accurately from various astronomical methods (e.g., Munk, 1997 and references therein; Cartwright, 1993; Ray, 1994; Kagan and Sundermann, 1996; Munk and Wunsch, 1998). In the last 10 years or so, these methods have converged on 3.7 TW for the total tidal dissipation in the Earth–Moon–Sun system. An estimated 0.2 TW of dissipation occurs in the solid-earth tides, leaving 3.5 TW to be dissipated in the oceans, with M_2 accounting for 2.4 TW. The geographical distribution of tidal dissipation has been a matter of longstanding interest. Taylor (1919) estimated 0.04 TW of dissipation in the Irish Sea from an area integral of $c_d \rho_0 \langle |\vec{u}|^3 \rangle$, where brackets denote time-averaging, the bulk drag coefficient $c_d = 0.0025$, $\rho_0 = 1035 \text{ kg m}^{-3}$ is the average density of seawater, and \vec{u} is the horizontal velocity vector. Jeffreys (1920) applied the method globally and estimated 2 TW of dissipation in all of the world's shallow seas. Miller (1966) arrived at a similar total dissipation but a rather different partition amongst the various shallow seas. Shallow seas cover a more limited area than the deep ocean but have much larger tidal velocities. Abyssal dissipations based on the nominal c_d value of 0.0025 would be two orders of magnitude too small to have a significant impact on the global dissipation budget (Munk, 1997).

The tidal power input P_{in} can be shown to equal the global integral

$$P_{\text{in}} = \rho_0 g \iint \left\langle \eta_{\text{EQ}} \frac{\partial \eta}{\partial t} \right\rangle dA, \quad (1)$$

(e.g., Egbert and Ray, 2001 and references therein), where t is time, the gravitational acceleration $g = 9.80 \text{ m s}^{-2}$, η_{EQ} is the equilibrium tide, to be discussed later, η is the surface tidal elevation with respect to mean resting water depths, and dA is an element of area. Since η_{EQ} is known to high accuracy and since data-constrained models have

accurate elevations, at least in the open ocean, several recent data-constrained models (Le Provost and Lyard, 1997; Kantha, 1998; Tierney et al., 2000) have globally integrated power inputs (and, therefore, dissipation rates, since there must be a balance in the time-average) that are in good agreement with the astronomical constraints. The spatial distribution of the dissipation, however, is not constrained by the global integral. Bulk-drag friction in the models cited above puts virtually all of the modeled dissipation into shallow seas. On the other hand, in-situ observations at specific locations (e.g. Armi, 1978; Polzin et al., 1997; Lueck and Mudge, 1997; Kunze and Toole, 1997; Ledwell et al., 2000) suggest that substantial energy dissipation occurs over mid-ocean rough topography. Ledwell et al. (2000) showed that the magnitude of column-integrated energy dissipation in Brazil Basin microstructure measurements modulates with the spring-neap cycle, suggesting that much of the dissipation is driven specifically by tides. Egbert and Ray (2000, 2001, 2003a) infer from T/P-constrained models that about 0.8 TW of M_2 dissipation, and 1 TW of dissipation across all constituents, occurs in the deep oceans, primarily over regions of rough topography.

Tidal flow over rough topography generates high-mode internal waves which break and dissipate, and low-mode internal tides (Wunsch, 1975; Hendry, 1977; Hendershott, 1981) which radiate. Relevant numerical and theoretical studies of internal wave and internal tide generation over rough topography include Cox and Sandstrom (1962), Baines (1973), Bell (1975a), Bell (1975b), Baines (1982), Hibiya (1986), Sjoberg and Stigebrandt (1992), Morozof (1995), Holloway (1996), Cummins and Oey (1997), Kantha and Tierney (1997), Holloway and Merrifield (1999), Kang et al. (2000), Merrifield et al. (2001), Niwa and Hibiya (2001), Balmforth et al. (2002), St. Laurent and Garrett (2002), Llewellyn Smith and Young (2002, 2003), Khatiwala (2003), St. Laurent et al. (2003), Legg (2004), and Polzin (2004). Some of the above studies are done in idealized conditions (e.g., Khatiwala, 2003). Some combine theories with velocity outputs from one-layer data-constrained models to estimate global barotropic to baroclinic conversion rates (e.g., Nycander, submitted 2004).

Some are realistic regional simulations (e.g., Holloway, 1996; Cummins and Oey, 1997; Kang et al., 2000; Merrifield et al., 2001). Niwa and Hibiya (2001) modeled the internal tides of the entire North Pacific. Coherent radiating low-mode internal tides have been found in acoustic tomography data (Dushaw et al., 1995) and in T/P data (Ray and Mitchum, 1996, 1997; Cummins et al., 2001), and a comprehensive observational and modeling study of the internal tides at Hawaii is described in Rudnick et al. (2003).

Consistent with JS, CL, and ERB, we show that the accuracy of forward-modeled tidal elevations depends to first order on the amount of parameterized abyssal dissipation. We show that even physically implausible drag schemes, such as the introduction of inordinately large bulk quadratic drag or horizontal viscosity coefficients, can produce reasonably accurate tides. However, following JS, CL, and ERB, we argue that topographic drag schemes are more physically plausible. Our topographic drag scheme is based on an exact linear solution for arbitrary terrain, augmented by a dimensional analysis to account for nonlinear drag due to bottom turbulence as well as linear drag due to radiating waves. In contrast to those in JS, but similar to those in ERB, our solutions are convergent with respect to iterations of the self-attraction and loading (SAL) term, and therefore represent self-consistent forward solutions for the global tide. As in JS, we perform multi-constituent forward model runs, whereas ERB focused on M_2 -only simulations. The regional and basin-wide studies of baroclinic tides previously noted have been done at high horizontal resolution (for instance, $1/10^\circ$ in Kang et al., 2000; 4 km in Merrifield et al., 2001, and $1/16^\circ$ in Niwa and Hibiya, 2001), and often include many vertical layers. We show here that even $1/2^\circ$ horizontal resolution and two layers in the vertical are enough to provide a useful result—namely, an improvement in the accuracy of surface tidal elevations over those in our one-layer model. In agreement with Ray and Mitchum (1996, 1997), we find that the direct signature of baroclinic tides on the surface elevation is small. The improvement in surface elevation accuracy in the two-layer model is due to a shift in the barotropic solution.

Our main focus is on tides in the open ocean. Coastal tides have smaller spatial scales than open-ocean tides, are more nonlinear, and exhibit aperiodic behaviors (Maas and Doelman, 2002). Obtaining accurate coastal tides in a global model is a formidable challenge which even data-constrained models are only beginning to meet (Ray, 1999; Tierney et al., 2000). We follow JS in referring to regions having resting water column depths less than 1000 m as “shallow” and regions having depths greater than 1000 m as “deep”, “abyssal”, “open-ocean”, or “mid-ocean”. The T/P-constrained model output we compare our forward model to was provided courtesy of R.D. Ray. We draw the four largest semidiurnal constituents (N_2 , M_2 , S_2 , and K_2) and four largest diurnal constituents (Q_1 , O_1 , P_1 , and K_1) from the GOT99.2 model (Ray, 1999), which is an empirical mapping guided by the Le Provost et al. (1994) results. Purely empirical derivations from T/P, documented in Egbert and Ray (2003b, see their Fig. 1a,b) provide us with the two largest long-period constituents (M_m and M_f). As with other recent forward tide models, our forward model contains one free parameter, associated with the topographic drag scheme. We tune this parameter to minimize the surface elevation discrepancy in M_2 -only runs with respect to GOT99.2, in deep waters over the latitudes covered by the T/P altimeter (66°S to 66°N). The optimal value of the free parameter so chosen is then used in multi-constituent runs. We compare the multi-constituent forward model elevations to those in the Ray results and to those in the set of 102 pelagic tide gauges used in Shum et al. (1997). Another test of our forward model can be made in latitudes poleward of 66° . Padman et al. (2002, 2003) and references therein present Antarctic tide models constrained by tide-gauge data, and Padman and Erofeeva (2004) and references therein present tide-gauge constrained Arctic tide models. Elevations in the global TPXO6.2 solution (Egbert and Erofeeva, 2002) compare well with Antarctic tide-gauge data (Laurie Padman, Gary Egbert, and Lana Erofeeva, personal communication 2004). We will therefore use TPXO6.2 as a benchmark in latitudes south of 66°S . The comparisons to pelagic tide gauges and to TPXO6.2 do not include

M_f and M_m . Against all three benchmarks, elevations in our forward two-layer model are more accurate than those in our one-layer model. Parameterized drag is needed to obtain accurate tides in both one- and two-layer simulations, and we provide a simple explanation for the sensitivity of elevation accuracy to drag. Although the main focus of this paper is on surface elevations, we also devote a brief section to the impact of baroclinicity on tidal velocities.

2. The model

2.1. Governing equations

We have adapted the Hallberg Isopycnal Model (HIM; Hallberg and Rhines, 1996) to be a forward model of tides. Our simulations are performed on a latitude–longitude grid running from 86°S to 82°N, which allows the possibility of accurate tidal modeling in the Antarctic, but not in the high Arctic. (Note that SHA utilizes a tripolar grid to perform truly global simulations.) Except where noted, the runs discussed in this paper are at 1/2° resolution. A few runs are at 1/4°. The one-layer mass conservation equation is

$$\frac{\partial \eta}{\partial t} + \nabla \cdot [(H + \eta)\vec{u}] = 0, \quad (2)$$

where H is the resting layer thickness (spatially varying, according to the topography). The one-layer momentum equation is

$$\begin{aligned} \frac{\partial \vec{u}}{\partial t} + (f + \zeta)\hat{k} \times \vec{u} \\ = -g\nabla(\eta - \eta_{EQ} - \eta_{SAL} - \eta_{MEM}) - \nabla \cdot \left(\frac{1}{2} \vec{u} \cdot \vec{u} \right) \\ + \frac{\nabla \cdot [K_H(H + \eta)\nabla \vec{u}]}{H + \eta} - \frac{c_d |\vec{u}| \vec{u}}{H + \eta} + \frac{\bar{T}\vec{u}}{\rho_0(H + \eta)}, \end{aligned} \quad (3)$$

where f is the Coriolis parameter, \hat{k} is a unit vector in the vertical direction, $\zeta = \hat{k} \cdot (\nabla \times \vec{u})$ is the vorticity, η_{EQ} is the equilibrium tidal forcing, η_{SAL} is the self-attraction and loading term, η_{MEM} is a “memory” term we have inserted which we discuss later, c_d is set to the canonical value of 0.0025

unless otherwise noted, K_H is a horizontal viscosity set to $10^3 \text{ m}^2 \text{ s}^{-1}$ unless otherwise noted, and \bar{T} is our topographic drag tensor, to be discussed later. The horizontal viscosity prevents sub-grid scale noise brought about by the non-linear advection terms in the governing equations (Egbert and Ray, 2003b), and prevents slow drifts in model energy. The chosen value of horizontal viscosity affects modeled energy dissipations at the level of a few percent or less.

The two-layer mass conservation equations are

$$\frac{\partial(\eta_1 - \eta_2)}{\partial t} + \nabla \cdot [(H_1 + \eta_1 - \eta_2)\vec{u}_1] = 0, \quad (4)$$

$$\frac{\partial \eta_2}{\partial t} + \nabla \cdot [(H_2 + \eta_2)\vec{u}_2] = 0, \quad (5)$$

and the momentum equations are

$$\begin{aligned} \frac{\partial \vec{u}_1}{\partial t} + (f + \zeta_1)\hat{k} \times \vec{u}_1 \\ = -g\nabla(\eta_1 - \eta_{EQ} - \eta_{SAL} - \eta_{MEM}) \\ - \nabla \cdot \left(\frac{1}{2} \vec{u}_1 \cdot \vec{u}_1 \right) + \frac{\nabla \cdot [K_H(H_1 + \eta_1 - \eta_2)\nabla \vec{u}_1]}{H_1 + \eta_1 - \eta_2}, \end{aligned} \quad (6)$$

$$\begin{aligned} \frac{\partial \vec{u}_2}{\partial t} + (f + \zeta_2)\hat{k} \times \vec{u}_2 \\ = -g\nabla(\eta_1 - \eta_{EQ} - \eta_{SAL} - \eta_{MEM}) \\ - g'\nabla(\eta_2 - \eta_{EQ} - \eta_{SAL} - \eta_{MEM}) \\ - \nabla \cdot \left(\frac{1}{2} \vec{u}_2 \cdot \vec{u}_2 \right) + \frac{\nabla \cdot [K_H(H_2 + \eta_2)\nabla \vec{u}_2]}{H_2 + \eta_2} \\ - \frac{c_d |\vec{u}_2| \vec{u}_2}{H_2 + \eta_2} + \frac{\bar{T}\vec{u}_2}{\rho_0(H_2 + \eta_2)}, \end{aligned} \quad (7)$$

where subscripts 1 and 2 denote upper and lower layers, respectively, H_1 and H_2 are the resting layer depths, η_1 and η_2 are the surface and interfacial height perturbations, and the reduced gravity $g' = (\rho_2 - \rho_1)/\rho_0$, where ρ_1 and ρ_2 are the layer densities. Note that we have chosen to have the drag tensor operating on the lower-layer flow.

Many references exist on the equilibrium tide η_{EQ} (e.g., Cartwright, 1977; Hendershott, 1981; Marchuk and Kagan, 1984; Pugh, 1987), which is astronomically forced but modified by a factor of $1 + k_2 - h_2$, where the Love numbers h_2 and k_2

Table 1

Constituent-dependent frequencies ω , astronomical forcing amplitudes A , and Love number factors $1 + k_2 - h_2$ used to compute equilibrium tide η_{EQ} . The periods $2\pi/\omega$ are also given

Constituent	ω (10^{-4} s^{-1})	A (cm)	$1 + k_2 - h_2$	Period (solar days)
M_m	0.026392	2.2191	0.693	27.5546
M_f	0.053234	4.2041	0.693	13.6608
Q_1	0.6495854	1.9273	0.695	1.1195
O_1	0.6759774	10.0661	0.695	1.0758
P_1	0.7252295	4.6848	0.706	1.0027
K_1	0.7292117	14.1565	0.736	0.9973
N_2	1.378797	4.6397	0.693	0.5274
M_2	1.405189	24.2334	0.693	0.5175
S_2	1.454441	11.2743	0.693	0.5000
K_2	1.458423	3.0684	0.693	0.4986

respectively account for the solid-earth body-tide deformation and the perturbation gravitational potential resulting from this deformation (Hendershott, 1972; Ray, 1998). Table 1, taken from documentation for the TPXO6.2 model (Egbert and Erofeeva, 2002), lists the frequencies, amplitudes, and Love numbers for the 10 constituents simulated in this paper. The frequencies and amplitudes are based on work by Doodson (1921), Cartwright and Tayler (1971), and Cartwright and Edden (1973)—a more recent computation was done by Roosbeek (1996). The Love numbers for the diurnal tides differ from those for the semi-diurnal and long-period tides because of the free-core nutation resonance (Wahr, 1981; Wahr and Sasao, 1981). When all 10 constituents are present, the equilibrium tide is

$$\begin{aligned}
 \eta_{\text{EQ}}(\phi, \lambda, t) &= \sum_l A(l)[1 + k_2(l) - h_2(l)] \\
 &\times \left(\frac{1}{2} - \frac{3}{2} \sin^2 \phi \right) \cos[\omega(l)t] \\
 &+ \sum_d A(d)[1 + k_2(d) - h_2(d)] \\
 &\times \sin(2\phi) \cos[\omega(d)t + \lambda] \\
 &+ \sum_s A(s)[1 + k_2(s) - h_2(s)] \cos^2 \phi \\
 &\times \cos[\omega(s)t + 2\lambda], \tag{8}
 \end{aligned}$$

where l is summed over M_m and M_f , d is summed over the four diurnal tides, s is summed over the four semi-diurnal tides, λ is longitude with respect to the Greenwich meridian, and ϕ is latitude. We set the time t to zero at the start of each numerical simulation. We ignore absolute time and slow modulations of phase or amplitude, all of which must be considered in more precise tidal analysis and prediction (e.g. Schwiderski, 1980; Pugh, 1987).

Most of our runs are M_2 -only or K_1 -only. In these cases we run the model for 20 days (equilibration typically takes about 12 days). All quantities discussed in this paper are drawn from the model after equilibration has been reached. Time averaged quantities are computed over a period of duration one forcing cycle, sampled every 12 min. Simulations of long-period tides require longer integrations. Frequencies are separated from each other in multi-constituent runs with the harmonic analysis package of Pawlowicz et al. (2002), which is based on that of Foreman (1977). Satisfaction of the Rayleigh criterion for separation of the K_2/S_2 and K_1/P_1 pairs requires an analysis period at least 182 days long. We run our multi-constituent simulations for 240 days, discard the first 40, and perform the harmonic analysis on the last 200. Because multi-constituent runs are time-consuming and computationally expensive, we perform only a few of them in this paper, after initial explorations have been done in single-constituent runs.

The perturbation potential due to the gravitational self-attraction of the ocean surface is

$$\sum_n \frac{3g\rho_0}{\rho_{\text{earth}}} \frac{\eta_n}{2n+1}, \quad (9)$$

where $\rho_{\text{earth}} = 5518 \text{ kg m}^{-3}$ is the average density of the solid earth and the η_n 's are order n spherical harmonics of the tidal elevation η (Hendershott, 1972; Ray, 1998). The solid earth yields to the load of the water column, and the gravitational potential is thus altered by the resulting redistribution of mass within the solid earth. The synthesis of these arguments is

$$\eta_{\text{SAL}} = \sum_n \frac{3\rho_0}{\rho_{\text{earth}}(2n+1)} (1 + k'_n - h'_n) \eta_n \quad (10)$$

(Hendershott, 1972; Ray, 1998). The load numbers h'_n and k'_n , introduced in Munk and MacDonald (1960), respectively account for solid-earth yielding and the resulting perturbation potential. We take the load numbers from Table A2 in Farrell (1972), who calculated them from a spherically symmetric solid-earth model. For our $1/2^\circ$ model, n goes from 1 to 360. We use a spline fit to fill in the gaps in Farrell's table. Usage of load numbers from more recent, but still spherically symmetric, solid-earth models (Jerry Mitrovica, 2003, personal communication) makes little difference to our tide model results.

Calculation of spherical harmonics as the numerical tide model is running is computationally infeasible. The simplest alternative is to use the "scalar approximation"

$$\eta_{\text{SAL}} \approx \beta \eta, \quad (11)$$

where β is a constant, often taken to be 0.085 (Accad and Pekeris, 1978). We estimate β by computing a least-squares fit in depths greater than 1000 m to η and η_{SAL} values in the GOT99 model. A representative value for the semi-diurnal tides is $\beta = 0.094$, and we use that as our nominal value. In some runs (i.e. those in Section 4.2) we use the scalar approximation and proceed no further. In some we begin with the scalar approximation and then employ the full formula (10) in an iterative procedure (Francis and Mazzega, 1990). In Section 4.1 we describe this procedure and the term η_{MEM} , which is introduced

into the momentum equation to force convergence of η_{SAL} (we set η_{MEM} to zero in all runs which employ the scalar approximation).

2.2. Diagnostics

The main diagnostic we use to evaluate model accuracy is the sea-surface height discrepancy D against benchmark elevations $\eta_{\text{BENCHMARK}}$, where the latter are drawn variously from GOT99.2, TPXO6.2, and the set of 102 pelagic tide gauges used in Shum et al. (1997):

$$D = \sqrt{\frac{\langle \iint (\eta - \eta_{\text{BENCHMARK}})^2 dA \rangle}{\iint dA}}. \quad (12)$$

Throughout the main body of this paper, brackets refer to time-averaging. When η and $\eta_{\text{BENCHMARK}}$ refer to the combined elevations of several constituents, we refer to D as the RSS (root-sum-square) discrepancy, as is customary in the literature. By computing the signal

$$S = \sqrt{\frac{\langle \iint (\eta_{\text{BENCHMARK}})^2 dA \rangle}{\iint dA}}, \quad (13)$$

we can compute relative errors, for instance, the percentage of sea surface height variance captured, given by $100 * [1 - (D/S)^2]$. As with D , S can be calculated either for individual constituents or for their (RSS) combination. Our calculations of D and S which utilize GOT99.2 or TPXO6.2 as benchmarks are restricted to deep waters (resting depths exceeding 1000 m). We also restrict our calculations of D and S to latitudes equatorward of 66° ; exceptions will be noted. In the pelagic tide gauge comparisons, as is customary, we compute averages that are not weighted by area or any other considerations.

The available potential energy (APE) and kinetic energy (KE) are given by

$$\begin{aligned} KE &= \frac{1}{2} \rho_0 \int \int (H + \eta) \vec{u} \cdot \vec{u} dA, \\ APE &= \frac{1}{2} \rho_0 g \int \int \eta^2 dA, \end{aligned} \quad (14)$$

in the one-layer case, and by

$$KE = \frac{1}{2} \iint [\rho_1(H_1 + \eta_1 - \eta_2)\vec{u}_1 \cdot \vec{u}_1 + \rho_2(H_2 + \eta_2)\vec{u}_2 \cdot \vec{u}_2] dA,$$

$$APE = \frac{1}{2} \rho_0 \iint (g\eta_1^2 + g'\eta_2^2) dA, \quad (15)$$

in the two-layer case. The kinetic energy can also be written as the sum of barotropic (BT) and baroclinic (BC) components $KE = KE_{BT} + KE_{BC}$, where

$$KE_{BT} = \frac{1}{2} \rho_0 \iint (H_1 + H_2 + \eta_1)\vec{u}_{BT} \cdot \vec{u}_{BT} dA,$$

$$KE_{BC} = \frac{1}{2} \rho_0 \iint (H_1 + H_2 + \eta_1)\vec{u}_{BC} \cdot \vec{u}_{BC} dA,$$

$$\vec{u}_{BT} = [(H_1 + \eta_1 - \eta_2)\vec{u}_1 + (H_2 + \eta_2)\vec{u}_2]/(H_1 + H_2 + \eta_1),$$

$$\vec{u}_{BC} = \sqrt{(H_1 + \eta_1 - \eta_2)(H_2 + \eta_2)} \times (\vec{u}_1 - \vec{u}_2)/(H_1 + H_2 + \eta_1). \quad (16)$$

In the latter case the second layer will not exist in waters shallower than $H_{\text{initupper}} - \eta_2$, where $H_{\text{initupper}}$ is the initial value of the upper layer thickness.

2.3. Input datasets

Our topographic drag scheme requires the Brunt–Vaisala frequency N at the seafloor, which we compute from the Levitus et al. (1998) climatology. Our bathymetry comes from a 2 min dataset assembled by Andrew Coward. Between 72°S and 72°N, Coward (2004, personal communication) mapped version 6.2 of the Smith and Sandwell (1997) dataset from the original Mercator projection onto a latitude–longitude grid by choosing median values over each model grid cell, without performing any smoothing. North of 72°N, an early version of the IBCAO (Jakobssen et al., 2000) dataset was used, without any smoothing at the joins, while ETOPO5 was joined without smoothing to the dataset south of 72°S. In waters that are south of 60°S and shallower than 1200 m, we alter Coward's dataset with data

obtained from Laurie Padman (2002, personal communication). The appendix in Padman et al. (2002) describes the sources of Antarctic bathymetry data. Under the Antarctic ice shelves, water depths are measured from the seafloor to the bottom of the ice.

The 1/30° topography $h_{\text{fine}}(x', y')$ is filtered onto the 1/2° and 1/4° grid values $H(x, y)$ via

$$H(x, y) = \frac{\iint h_{\text{fine}}(x', y') F(x, y, x', y') dA}{\iint F(x, y, x', y') dA}. \quad (17)$$

We use a radial Blackman filter

$$F(x, y, x', y') = 0.42 + 0.5 \cos(\pi r_{\text{field}}/r_{\text{filter}}) + 0.08 \cos(2\pi r_{\text{field}}/r_{\text{filter}}), \quad (18)$$

where $r_{\text{field}} = \sqrt{(x - x')^2 + (y - y')^2}$ is the distance from the coarse grid model gridpoint (x, y) to the field point (x', y') , and r_{filter} is the filter radius. For points lying outside the filter radius, $F=0$. After some initial explorations, we chose a filter radius of 55 km (1/2° in latitude) to prepare both the 1/2° and 1/4° model grids used in this paper. Thus both grids have the same amount of roughness. The chosen 55 km filter radius does not satisfy the Nyquist criteria for the 1/2° simulations, which therefore contain noticeably more gridscale noise than the 1/4° simulations, in both the surface and interfacial elevation fields. However, in both the one- and two-layer runs, elevation accuracy is nearly equal in 1/2° as 1/4° simulations. The model elevation accuracy is sensitive to the type (e.g., Gaussian versus Blackman) and radius of the filter used to map the topography onto our model grid. The sensitivity to the preparation of the topographic grid, and the related sensitivity to resolution, will be further explored in a future paper.

3. Summary of topographic drag scheme

The classic topographic drag problem has a steady flow \vec{u} over small-amplitude topography $h \sin(kx)$, where h and k are constants, the fluid has constant Brunt–Vaisala frequency N , and the internal wave drag is $\rho_0 N k h^2 \vec{u}$. Actual ocean topography contains a spectrum of heights and wavenumbers. For their forward tidal model, JS

first calculated the water depths H at every gridpoint in their $1/2^\circ$ domain by fitting a polynomial through all the $1/30^\circ$ Smith and Sandwell (1997) data contained by the coarse model gridpoint. The rms of the residuals of the nearby $1/30^\circ$ heights with respect to the local H is taken to be the roughness h . JS added a factor of $\frac{1}{2}$ to the formula above, and then tuned k to minimize the misfit between their forward modeled elevations and those of data-constrained models.

In this section we summarize our topographic drag scheme (Garner, 2003; also, submitted 2004), which was originally developed for quasi-steady background flows in the atmosphere, and then extended to the oscillatory case relevant for tides. Details of the scheme are provided in the Appendix. Instead of using statistical measures of the various vertical and horizontal scales in the topography, the scheme is based on an exact analytical solution for drag in the hydrostatic limit over arbitrary small-amplitude terrain $h(\vec{x})$. The drag in the oscillatory case depends on tidal frequency. Since M_2 is the dominant tidal constituent, we tune our drag scheme in M_2 -only runs and use the resulting optimal drag parameter in the drag formula for our multi-constituent runs. Our application of the drag scheme is therefore not strictly correct for the diurnal and long-period tides in such runs. However, the accuracy of diurnal tidal elevations is not as sensitive to drag as is the accuracy of semi-diurnal elevations, and the accuracy of long-period elevations exhibits very little sensitivity.

Inspired by the meteorological literature on topographic drag and drag parameterizations (e.g., Pierrehumbert, 1987; Miranda and James, 1992; Lott and Miller, 1997), we employ dimensional reasoning in our scheme to accommodate the possibility of drag due to low-level wave breaking and turbulence as well as that due to linear radiating waves. Waves radiating away from small mountains or the tips of tall mountains cause drag proportional to $|\vec{u}|$, while low-level breaking in flow deflected around tall mountains causes drag proportional to $|\vec{u}|^2$. Flow splitting occurs when a nondimensional parameter exceeds an order one critical value. The measure of nonlinearity depends on whether or not the topo-

graphic length scales considered are small enough that oscillatory flows appear to be “steady”. The nonlinearity measure for large scales is small, indicating that flow splitting and nonlinear drag probably occur mostly at small scales. The nonlinearity parameter for small scales is the Froude number $Nh/|\vec{u}|$. Thurnherr and Richards (2001), Thurnherr et al. (2002), and Thurnherr and Speer (2003) argue from observational data that turbulence associated with hydraulic jumps occurs in areas of rough topography when the Froude number exceeds an order one threshold. The end products of our dimensional reasoning are a “propagating” drag D_p due to radiating waves (which presumably break above the topography) and a “non-propagating” drag D_{np} due to low-level turbulence. Our scheme takes the drag direction from the linear analysis, and matches the small amplitude limit of D_p to the linear analytical result. The final result for our drag is given in the Appendix.

In all of the runs presented in this paper, our drag scheme operates in waters 1000 m and deeper. JS used their scheme in waters 100 m and deeper. Preliminary investigations indicate that the accuracy of our forward-modeled tidal elevations improves slightly if we use our drag scheme in waters 100 m and deeper, and our future work may implement this. The horizontal length scale over which to compute the quantity χ defined in the Appendix (Eq. (31)) is another ambiguous parameter. Larger integration scales lead to larger values of χ and thus drag. We choose to integrate (31) over 40 km, which is an order-one fraction of the order 100 km topographic length scales involved in generating the first-mode baroclinic tide (see Fig. 11 in SHA). Topographic scales much larger than this do not generate internal waves and should not be included.

Much of the turbulent kinetic energy dissipation seen in microstructure data (Lou St. Laurent, 2003, personal communication) occurs within 500 m of the bottom. Internal waves with vertical scales much smaller than this are generated by horizontal topographic scales of order hundreds of meters to a few kilometers. Although the Smith and Sandwell (1997) topographic dataset is mapped onto a $1/30^\circ$ grid, its true horizontal

resolution is of order π times the ocean depth, i.e. about 12 km. Thus the Smith and Sandwell dataset is missing the horizontal scales that generate breaking high-mode internal waves (and low-level turbulence). We have found that our estimated topographic drag must be augmented by a multiplicative factor to obtain accurate tidal elevations. We tune the multiplicative factor to minimize D . Our present interpretation is that the multiplicative factor makes up for the missing scales in the topographic dataset, but we will examine this assumption more closely in future work. We stress again that JS also had a tunable parameter (k). We show that both schemes, when optimally tuned, produce nearly identical overall levels of drag, as measured by the spatially-averaged decay rate. In our one-layer runs, the spatially averaged decay rate is

$$r_{\text{average}} = \frac{\iint \left(\left| \frac{\bar{T}\bar{u}}{\rho_0(H+\eta)} \right| / |\bar{u}| \right) dA}{\iint dA}. \quad (19)$$

For the JS scheme the spatially averaged decay rate is

$$r_{\text{average}} = \frac{\iint (kh^2 N / 2H) dA}{\iint dA}. \quad (20)$$

4. Surface elevation accuracy of M_2 -only simulations

This section explores the surface elevation accuracy in M_2 -only simulations. We examine the effects of self-attraction and loading in one-layer runs, and the effects of parameterized drag in both one- and two-layer runs. The results of the exploration are utilized in the multi-constituent runs of the next section.

4.1. Effects of self-attraction and loading

Although the amplitude of η_{SAL} is only about one-tenth that of η , $\nabla\eta_{\text{SAL}}$ is an order-one perturbation in the momentum equation because η_{SAL} contains much smaller scales than does η_{EQ} (Hendershott, 1972; Gordeev et al., 1977). To

confirm the critical importance of this term, we performed $1/2^\circ$ M_2 -only simulations which completely omit η_{SAL} . Our topographic drag scheme was used, augmented by a multiplicative factor tuned as described in the next subsection. The minimum D value was 19.32 cm, much larger than that obtained when the scalar approximation (11) or the full expression (10) is used for η_{SAL} . In K_1 -only simulations which omit the η_{SAL} term, the elevation errors against GOT99.2 were also substantially larger than in simulations which employ the scalar approximation, although the difference between the two cases is not as dramatic as it is with M_2 .

We now describe our procedure for iterating η_{SAL} past the scalar approximation, in $1/2^\circ$ runs which employ an optimally tuned topographic drag scheme. Once the first iteration, employing the scalar approximation, is completed, η_{SAL} is calculated offline from the model output via (10). Amplitude and phase maps $A_{\text{SAL}}(\phi, \lambda)$ and $p_{\text{SAL}}(\phi, \lambda)$ are created which satisfy

$$\eta_{\text{SAL}}(\phi, \lambda, t) = A_{\text{SAL}}(\phi, \lambda) \cos[\omega t - p_{\text{SAL}}(\phi, \lambda)]. \quad (21)$$

As is standard, the phase is referenced to the Greenwich meridian. The next iteration of the model computes η_{SAL} from the amplitude and phase maps made from the first iteration. When the new iteration is complete, new maps (21) are again created offline for use in the following iteration. Convergence can be obtained with this straightforward iteration technique in K_1 -only simulations, but in M_2 -only runs the value of D oscillates (solid curve in Fig. 1). Similar oscillations were seen by JS, who consequently averaged their model results over the iterations (Steve Jayne, 2003, personal communication). We have been able to suppress the oscillations by employing “memory” of the tidal elevations in previous iterations. Let us denote the tidal elevations of the iteration just before the current iteration by η_{PREVIOUS} . We construct amplitude maps $A_{\text{PREVIOUS}}(\phi, \lambda)$ and phase maps $p_{\text{PREVIOUS}}(\phi, \lambda)$ for this quantity and store them for use in the current iteration:

$$\eta_{\text{PREVIOUS}}(\phi, \lambda, t) = A_{\text{PREVIOUS}}(\phi, \lambda) \times \cos[\omega t - p_{\text{PREVIOUS}}(\phi, \lambda)]. \quad (22)$$

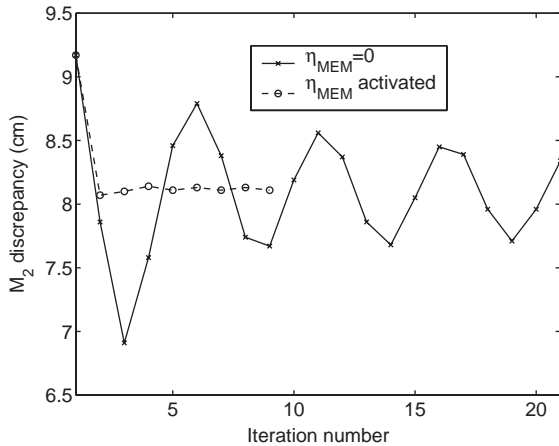


Fig. 1. Time- and area-averaged sea-level discrepancy D against GOT99.2 in iterations of $1/2^\circ$ one-layer M_2 -only runs, done with and without η_{MEM} . Discrepancies are calculated in waters deeper than 1000 m and equatorward of 66° . Iterations are with respect to η_{SAL} , the self-attraction and loading term.

For each iteration, we set η_{MEM} to be 0.094 (the same constant used in the scalar approximation) times the departure of the tide η in the current iteration from the elevation $\eta_{PREVIOUS}$ in the previous iteration:

$$\eta_{MEM} = 0.094(\eta - \eta_{PREVIOUS}). \quad (23)$$

With this technique, the sea-surface height discrepancy converges quickly (dashed curve in Fig. 1). Once the solution has converged, η_{MEM} is by definition a small term. Indeed, we found that when we continued the converged series plotted in Fig. 1, but with the η_{MEM} term removed, the discrepancies remain at the same level. Therefore it is not necessary to retain η_{MEM} past the first few iterations. ERB (see also references therein) also found that their iterations of η_{SAL} did not converge, unless an equivalent modified iteration procedure was employed.

The elevation error in the third iteration of our $\eta_{MEM} = 0$ set is substantially lower than that in the other iterations including all iterations in the convergent set. However, since the error does not remain at this low level, the third iteration in the $\eta_{MEM} = 0$ set is not a self-consistent solution. We believe therefore that the low error should be considered fortuitous. Using values of β other than

0.094 in (11) can also yield solutions with low elevation discrepancies. However, in these latter cases the discrepancy increases once η_{SAL} is iterated using the proper formula, and we believe the low discrepancies should again be considered fortuitous. In succeeding sections, whenever the self-attraction and loading term is iterated beyond the scalar approximation, η_{MEM} is employed, and the solutions are self-consistent.

4.2. Effects of parameterized drag in one-layer runs

This subsection explores the effects of parameterized drag on the accuracy of tidal elevations in one-layer $1/2^\circ$ M_2 -only experiments which, except where noted, employ the scalar approximation $\eta_{SAL} = 0.094\eta$ for simplicity. Even physically implausible drag can improve forward model accuracy. Fig. 2(A) plots the time-averaged global APE and KE in simulations which have no topographic drag, but in which c_d is treated as a tunable parameter. Both APE and KE decrease as c_d is increased. Fig. 2(B) shows the sea-surface height discrepancy D of the same experiments with respect to GOT99.2, computed in waters deeper than 1000 m and over latitudes equatorward of 66° . Since APE is the global integral of η^2 , a quantity clearly related to D , we expect experiments with APE near that of observations to have relatively small elevation errors. Inspection of Fig. 2 indicates that this is the case. Thus drag affects surface elevation accuracy simply because it controls tidal amplitudes. The optimal experiment in Fig. 2 has a c_d value of 0.64, 256 times larger than the nominal value, which places significant dissipation (1.56 TW; see SHA for details of the model energy budget analysis) into the abyss and yields a total M_2 dissipation across deep and shallow waters of 3.09 TW, somewhat higher than the observed 2.44 TW value. Fig. 3 displays

$\sqrt{\langle (\eta - \eta_{GOT99.2})^2 \rangle}$, the spatial pattern of the temporally averaged M_2 elevation discrepancies, for both the nominal and optimal c_d experiments. Both experiments shown in this figure were iterated with respect to the self-attraction and loading term via the procedure described in Section 4.1. The amount of drag clearly affects

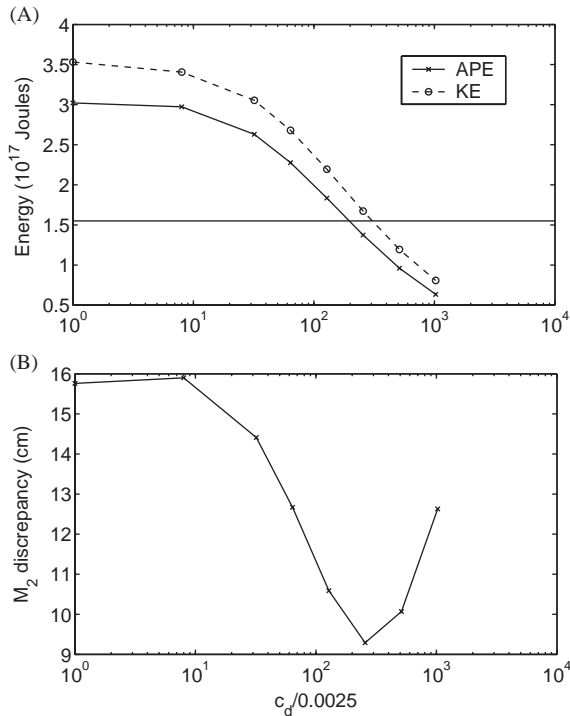


Fig. 2. (A) Global APE and KE in $1/2^\circ$ one-layer M_2 -only simulations with $\eta_{\text{SAL}} = 0.094\eta$ and variable c_d . The extra horizontal line represents the observed value of APE, taken from Tierney et al. (2000). (B) Time- and area-averaged sea-level discrepancy D against GOT99.2, in waters deeper than 1000 m and equatorward of 66° .

the spatial distribution as well as the magnitude of error. APE and D are similarly sensitive to the value of K_H in experiments (not shown) which treat it as a tunable parameter while omitting topographic drag. The optimal K_H in terms of producing accurate elevations is $4.5 \times 10^5 \text{ m}^2 \text{ s}^{-1}$. Again, this is at least two orders of magnitude larger than any physically plausible value.

The tunable c_d and tunable K_H simulations described above demonstrate that tidal amplitudes and thus accuracies are sensitive to drag, even if this drag is physically implausible. Fig. 4 shows that the same principles hold when we tune the multiplicative factor augmenting our topographic drag scheme, which is physically motivated, and concentrates parameterized dissipation into regions of rough topography (Fig. 5), in accordance with in situ (Polzin et al., 1997) and satellite

(Egbert and Ray, 2000, 2001, 2003a) observations. Fig. 6 shows the spatial pattern of the elevation discrepancies against GOT99.2 in the optimally tuned one-layer M_2 -only simulation. Again, as in Fig. 3, the simulations shown in Figs. 5 and 6 were iterated with respect to η_{SAL} . The optimal multiplicative factor for the iterated solutions is 7, lower than the optimal factor of 9 in runs employing the scalar approximation. Although the globally averaged elevation error is not much lower than that in the $c_d = 0.64$ run, the spatial distribution of error is different. The global tidal solution is affected by the spatially distributed nature of the topographic drag as well as its total magnitude.

4.3. Effects of parameterized drag in two-layer runs

To match the stratification of the ocean most closely in a two-layer simulation, one might choose a target density surface near the bottom of the thermocline and initialize its depths in the model according to a climatology. However, since such an interface would slope in the horizontal, it would undergo geostrophic adjustment in the absence of forcing which could maintain it. For simplicity, we instead choose to initialize our two-layer run with an interface placed uniformly at 700 m throughout the model domain. For similar reasons, we choose one representative value of g' , $1.64 \times 10^{-2} \text{ m s}^{-2}$, estimated for realistic subtropical gyre conditions from a formula in Flierl (1978) that depends on the chosen 700 m interfacial depth. We found that the elevation discrepancies D are not strongly sensitive to the exact value of g' , which we varied from $1.2 \times 10^{-2} \text{ m s}^{-2}$ to $1.8 \times 10^{-2} \text{ m s}^{-2}$, or to the exact placement of the interfacial depth, which we varied from 600 to 900 m. Visual inspection of the interfacial waves indicates that they are marginally resolved in $1/2^\circ$ runs, especially with smaller g' values, which render smaller horizontal scales. Two-layer $1/4^\circ$ M_2 -only experiments resolve the interfacial waves much better but yield nearly identical elevation errors.

It is an interesting question whether our drag parameterization should be thought of as representing conversion to low baroclinic modes or to high ones. This question takes on particular interest in our two-layer simulations, in which we

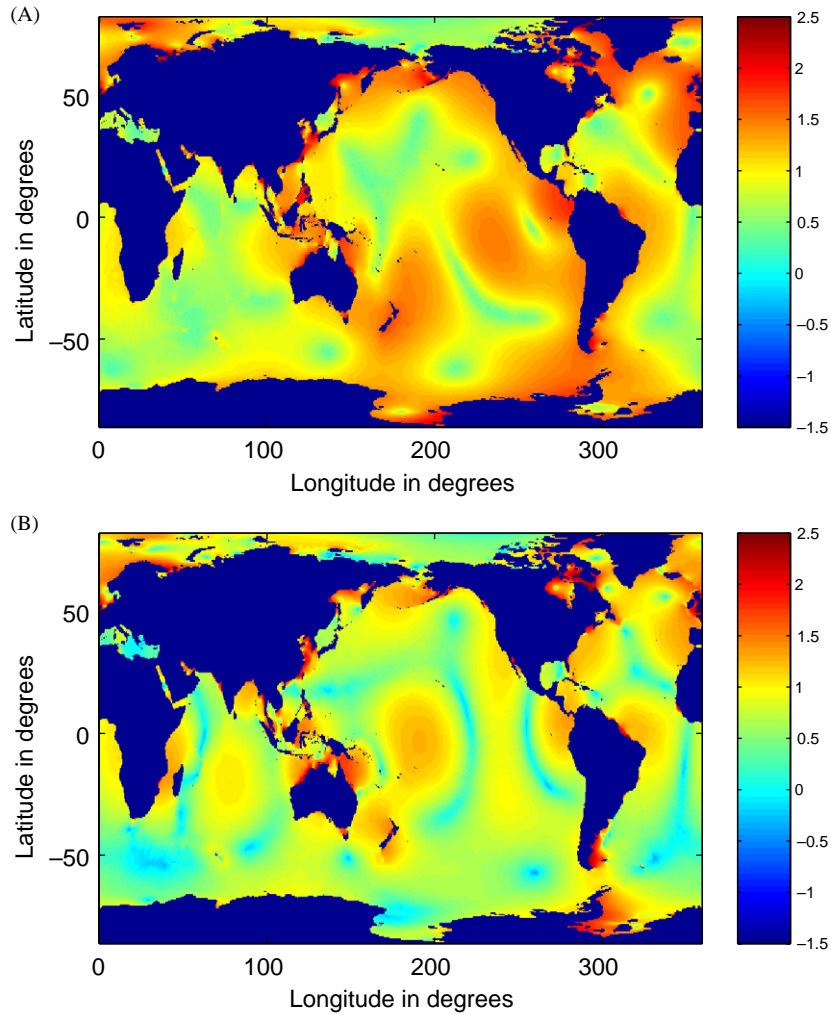


Fig. 3. Log₁₀ of time-averaged sea level errors $\sqrt{\langle(\eta - \eta_{\text{GOT99.2}})^2\rangle}$ (in cm) for 1/2° one-layer M₂-only: (A) $c_d = 0.0025$ experiment and (B) $c_d = 0.64$ experiment.

resolve the generation of the first baroclinic mode internal tide. Our initial expectation therefore was that less parameterized drag would be required to obtain accurate surface elevations in two-layer experiments. However, the sensitivity of two-layer M₂ simulations to the multiplicative factor is similar to the sensitivity in one-layer experiments. Two-layer M₂-only, 1/4° experiments having no parameterized topographic drag (i.e., only a c_d value of 0.0025 for dissipation) yield an rms elevation error of 12.8 cm (against GOT99.2, in waters deeper than 1000 m and equatorward of

66°) when the full iteration of self-attraction and loading is used. This represents an improvement over the 14.9 cm error we obtain in a nominal c_d -only one-layer run, but is much larger than the 7.4 cm error obtained with an optimally tuned multiplicative factor. The optimal multiplicative factor of 8 is not much different from the optimal factor of 7 found in one-layer simulations. Our preliminary interpretation of this fact is as follows. As was shown in the previous subsection, energy must be taken out of the system, via parameterized drag in the abyss, in order to bring about accurate

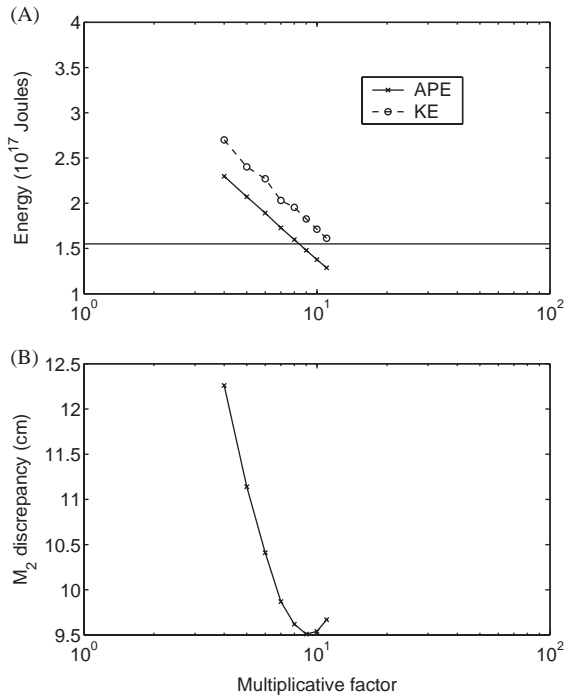


Fig. 4. (A) Global APE and KE in $1/2^\circ$ one-layer M_2 -only simulations with $\eta_{\text{SAL}} = 0.094\eta$, run with our topographic drag scheme augmented by a variable multiplicative factor. The extra horizontal line represents the observed value of APE, taken from Tierney et al. (2000). (B) Time- and area-averaged sea-level discrepancy D against GOT99.2, in waters deeper than 1000 m and equatorward of 66° .

tidal energies and elevations. In two-layer experiments, a substantial amount of energy is converted from the barotropic to the baroclinic tide, as SHA shows. However, low-mode generation is an internal, adiabatic conversion, and, unlike parameterized drag, does not directly remove energy from the system as a whole. It is computationally infeasible for our hydrostatic, two-layer model to resolve the generation and breaking of internal waves at very small scales. Hence the need apparently remains for parameterized drag, which we have acting on the lower layer flow rather than the barotropic flow. Since the vertically integrated kinetic energy in the one- and two-layer simulations is the same to within 10 percent, the amount of parameterized drag required to obtain accurate tides is similar in the two cases.

5. Surface elevation accuracy of multi-constituent simulations

In the two subsections to follow we discuss the surface elevation accuracy of a $1/2^\circ$ one-layer ten-constituent simulation and a $1/2^\circ$ two-layer ten-constituent simulation. Both employ η_{MEM} to iterate the self-attraction and loading term. In both cases, sea-surface height discrepancies against the Ray results were very similar in the second and third iterations, and we take results from the third iteration. Our topographic drag scheme was used, augmented by a multiplicative factor of 7 in the one-layer case and 8 in the two-layer case.

5.1. One-layer multi-constituent run

The third column of Table 2 lists values of D in the one-layer run, measured against the Ray data in deep waters equatorward of 66° . The signal S for each constituent is given in the second column. The RSS anomaly of all the constituents is 9.54 cm, slightly lower than the 10.1 cm found by JS. Our M_2 and S_2 elevation discrepancies are slightly higher than those in JS. Numbers in parentheses denote percentage of sea-surface height variance captured. Although the discrepancies for the various constituents differ greatly in absolute terms, the percent variance captured is confined to a relatively narrow range (83.8–94.4) across the constituents. In contrast, the K_1 , O_1 , P_1 , and Q_1 solutions in JS capture 67, 81, 80, and 25 percent of the variance, respectively. In terms of percent variance captured, our semi-diurnal constituents, especially S_2 and K_2 , are less accurate than our diurnal tides. Our relatively poor S_2 results may be due to the air tide forcing at that frequency, which we have not accounted for (Rui Ponte and Gary Egbert, personal communication 2004). The percent variance captured is also relatively low for M_m and M_f . This is probably due to contamination by other low-frequency oceanic motions (Desai et al., 1997; Egbert and Ray, 2003b) in the Ray data, rather than to any inherent difficulty in simulating long-period tides. Our long-period elevations match those in the forward long-period simulations of Egbert and Ray (2003b) much more closely. The elevation

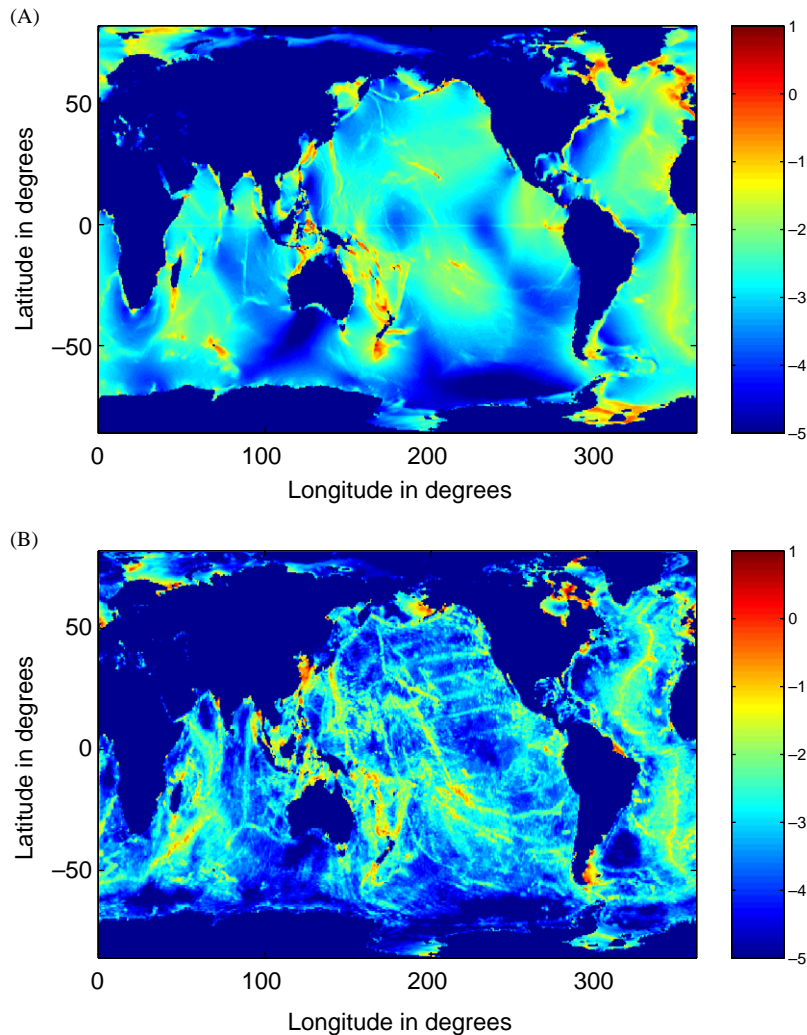


Fig. 5. Log_{10} of time-averaged parameterized dissipation (in W m^{-2}) in $1/2^\circ$ one-layer M_2 -only run with (A) optimally tuned c_d value of 0.64 and (B) optimally tuned topographic drag scheme (multiplicative factor of 7).

discrepancies of the four semi-diurnal and four diurnal constituents in our one-layer forward model are all slightly lower when measured against TPXO6.2 than when measured against GOT99.2, such that the RSS reduces from 9.54 to 9.42 cm.

Elevation discrepancies against the set of 102 pelagic tide gauges are shown in Table 3. For the sake of comparison, the (much lower) GOT99.2 discrepancies with the tide gauge data are also shown. The elevation errors of our one-layer forward model against tide gauges are larger than

the errors against GOT99.2 for all constituents except K_2 . However, across all constituents, the signal sampled by the gauges is larger than the globally averaged signal (compare the second columns of Tables 2 and 3), such that the percent of the RSS signal variance captured is slightly higher (91.9 versus 91.0 percent) when tide gauges are used as the benchmark. As in the comparisons with GOT99.2, our model captures diurnal elevations better than semidiurnal elevations, and again the poorest performance is in S_2 and K_2 . The

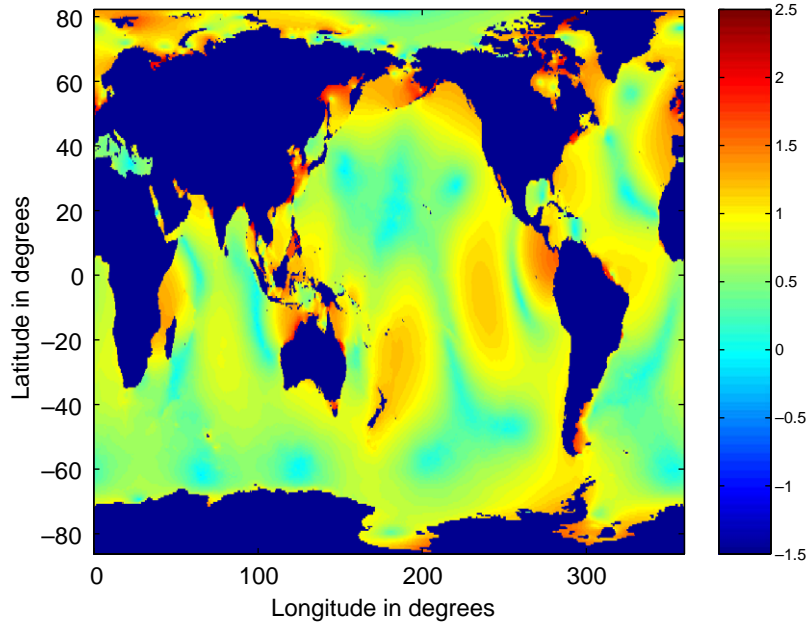


Fig. 6. Log_{10} of time-averaged sea level errors $\sqrt{\langle(\eta - \eta_{\text{GOT99.2}})^2\rangle}$ (in cm) for $1/2^\circ$ one-layer M_2 -only experiment having topographic drag with multiplicative factor of 7.

Table 2

Second column: time- and area-averaged sea-surface height signals S calculated from GOT99.2 (for the diurnals and semi-diurnals) and from empirical mappings (for M_f and M_m). Third and fourth columns: Time- and area-averaged sea-surface height discrepancies D of $1/2^\circ$ multi-constituent one- and two-layer forward simulations with respect to GOT99.2 (for the diurnals and semi-diurnals) and to the empirical mappings (for M_f and M_m).

Constituent	Signal S (cm)	One-layer D (cm)	Two-layer D (cm)
M_m	0.49	0.17 (87.3)	0.17 (87.3)
M_f	0.90	0.27 (91.0)	0.28 (90.0)
Q_1	1.39	0.36 (93.2)	0.38 (92.7)
O_1	6.61	1.57 (94.4)	1.53 (94.7)
P_1	3.13	0.77 (93.9)	0.64 (95.9)
K_1	9.54	2.45 (93.4)	1.88 (96.1)
N_2	5.65	1.51 (92.9)	1.37 (94.1)
M_2	26.69	7.76 (91.6)	7.26 (92.6)
S_2	10.57	4.26 (83.8)	4.12 (84.8)
K_2	2.97	1.08 (86.8)	1.05 (87.6)
RSS	31.82	9.54 (91.0)	8.90 (92.2)

All quantities are computed in waters deeper than 1000m and equatorward of 66° . Numbers in parentheses denote percentage of sea-surface height variance captured in the forward simulations.

fourth column of Table 4 lists the elevation discrepancies of our one-layer forward model against TPXO6.2 in waters deeper than 1000m and latitudes south of 66°S . For comparison, the

TPXO6.2 signals, and the discrepancies between GOT99.2 and TPXO6.2, are also listed. In this comparison, once again we fare better with diurnal tides than with semidiurnal tides. However, the

Table 3

Time and station-averaged sea-surface height signals S at the set of 102 pelagic tide gauges used in Shum et al. (1997), and sea-surface height discrepancies D of GOT99.2 and of our $1/2^\circ$ multi-constituent one- and two-layer forward simulations with respect to the gauges

Constituent	Signal S (cm)	GOT99.2 D (cm)	One-layer D (cm)	Two-layer D (cm)
Q_1	1.62	0.28	0.43 (92.8)	0.40 (93.9)
O_1	7.76	0.89	1.79 (94.7)	1.62 (95.7)
P_1	3.62	0.37	0.84 (94.6)	0.73 (95.9)
K_1	11.26	1.02	2.90 (93.3)	2.26 (96.0)
N_2	6.86	0.65	1.95 (91.9)	1.83 (92.9)
M_2	33.22	1.48	9.33 (92.1)	8.75 (93.1)
S_2	12.62	1.03	4.44 (87.6)	4.25 (88.7)
K_2	3.43	0.43	1.00 (91.4)	0.96 (92.2)
RSS	39.04	2.43	11.14 (91.9)	10.36 (93.0)

Numbers in parentheses denote percentage of sea-surface height variance captured in the forward simulations. Our calculated GOT99.2 discrepancies agree with those in Table 2 of Ray (1999), except that he applied an air tide correction to the bottom pressure recorder S_2 data which reduces the S_2 discrepancy to 0.94 cm. The air tide correction is not present in the Shum et al. dataset we used.

Table 4

Southern ocean time- and area-averaged sea-surface height signals S calculated from TPXO6.2 and sea-surface height discrepancies D of GOT99.2 and of our $1/2^\circ$ multi-constituent one- and two-layer forward simulations with respect to TPXO6.2

Constituent	Signal S (cm)	GOT99.2 D (cm)	One-layer D (cm)	Two-layer D (cm)
Q_1	3.79	0.40	0.50 (98.2)	0.41 (98.8)
O_1	17.60	3.89	2.11 (98.6)	1.72 (99.0)
P_1	5.73	0.90	1.52 (93.0)	0.78 (98.1)
K_1	18.11	2.66	5.06 (92.2)	2.53 (98.1)
N_2	3.63	0.94	1.52 (82.4)	1.36 (86.0)
M_2	18.96	2.01	6.75 (87.3)	5.99 (90.0)
S_2	13.35	1.04	5.09 (85.5)	5.05 (85.7)
K_2	3.79	0.41	1.36 (87.1)	1.32 (88.0)
RSS	35.36	5.41	10.40 (91.4)	8.66 (94.0)

All quantities are computed in waters deeper than 1000 m and south of 66°S . Numbers in parentheses denote percentage of sea-surface height variance captured in the forward simulations.

difference is more striking in the Antarctic. The semi-diurnal constituents are never captured at better than 87.3 percent, while the diurnal constituents are all captured at 92.2 percent or better.

Table 5 lists the global tidal working rates computed from T/P-constrained models by Egbert and Ray (2003a) alongside the working rates, computed from (1) over all model gridpoints (deep and shallow), in our one-layer multi-constituent run. With the exception of the Q_1 rate, our one-layer forward model working rates match those in the T/P-constrained models to within 8 percent or better. The largest discrepancy is in the M_2 rate,

which is 0.2 TW too large, as is the total rate summed over all constituents. A rough estimate of the parameterized dissipation in the abyss of our multi-constituent run can be made by assuming that the topographic drag decay rate is spatially uniform, so that the last term in (3) is $-r\vec{u}$ rather than $\overline{T\vec{u}}/\rho_0(H+\eta)$. Multiplication of $-r\vec{u}$ by $\rho_0(H+\eta)\vec{u}$ and global integration would yield $-\rho_0 r \iint (H+\eta)\vec{u} \cdot \vec{u} dA = -2r \text{KE}$ for the decay rate of tidal energy. The spatially-averaged decay rate computed from (19) in waters deeper than 1000 m when the optimal multiplicative factor of 7 is used is $(2.0 \text{ days})^{-1}$, very close to the

Table 5
The global working rates of the tidal constituents

Constituent	Egbert and Ray global work (TW)	One-layer global work (TW)	Two-layer global work (TW)
Q ₁	0.007	0.008 (+14)	0.009 (+29)
O ₁	0.173	0.181 (+5)	0.198 (+14)
P ₁	0.035	0.034 (−3)	0.034 (−3)
K ₁	0.343	0.329 (−4)	0.334 (−3)
N ₂	0.110	0.115 (+5)	0.114 (+4)
M ₂	2.435	2.632 (+8)	2.577 (+6)
S ₂	0.376	0.392 (+4)	0.380 (+1)
K ₂	0.030	0.029 (−3)	0.028 (−7)
Total	3.508	3.719 (+6)	3.672 (+5)

The second column is from Table 1 of Egbert and Ray (2003a), computed from data-constrained solutions. The third and fourth columns are the workings in our 1/2° one- and two-layer multi-constituent forward simulations. Numbers in parentheses indicate the percentage differences of the model results with respect to the Egbert and Ray results.

(2.1 days)^{−1} rate computed from (20) in the optimal run in JS. If one multiplies (2.0 days)^{−1} by twice the abyssal model kinetic energy in our optimally tuned one-layer multi-constituent experiment, one estimates 2.3 TW for the parameterized abyssal dissipation. This is slightly larger than the 1.85 TW abyssal dissipation we compute from an energy budget analysis (see SHA for details) of our one-layer multi-constituent run. The energy budget analysis provides working and dissipation rates at every model gridpoint, as the model is running, while (1) holds only when integrated globally. The energy budget analysis thus yields a working rate that is independent from that obtained by summing the constituent values obtained via (1). The two estimates of the global total working rates agree with each other and with the global total dissipation estimate to better than 0.01 TW. The energy budget is computed through multiplication of the momentum equation by $(H + \eta)\bar{u}$ as the model is running, and hence does not separate out the constituents. The abyssal dissipations in our one-layer model are significantly larger than those found by Egbert and Ray (2000, 2001, 2003a) in T/P-constrained solutions, and by the JS and ERB one-layer forward models.

5.2. Two-layer multi-constituent run

The fourth column of Table 2 lists the elevation discrepancies against the Ray results in our two-

layer multi-constituent run. The discrepancies are lower than those in the one-layer multi-constituent run across all constituents save the three smallest. The RSS error over all constituents is reduced from 9.54 to 8.90 cm (or, from 9.42 to 8.78 cm when measured against TPXO6.2). Again, the semi-diurnal tides, especially S₂ and K₂, are less accurate (in terms of percentage of sea-surface height variance captured) than the diurnal tides. Table 3 shows that the improvement in elevation accuracies in the two-layer forward model over the one-layer forward model also holds when pelagic tide gauges are used as the benchmark. The addition of another layer yields an extra percent of sea surface height variance captured in the RSS signal, just as it does when elevations are measured against GOT99.2. Table 4 shows that the inclusion of another layer also lowers elevation errors across all constituents when TPXO6.2 is used as a benchmark in waters deeper than 1000 m and south of 66°S. The increase in percent variance captured is greatest for P₁ and K₁, as it was when measuring the one and two layer models against the other two benchmarks. The diurnal elevations in the two-layer forward model match the TPXO6.2 elevations in the open Antarctic at the level of 98 to 99 percent variance captured. The P₁ and K₁ elevations in GOT99.2 match those in TPXO6.2 slightly less well in the Antarctic than do the P₁ and K₁ elevations in our two-layer forward simulations, and our two-layer model apparently

captures the O_1 elevations significantly better. The GOT99.2 semi-diurnal elevations match TPXO6.2 much more closely than do the semi-diurnal elevations in our forward model. With the notable exception of the O_1 global working rate, the constituent global working rates of the two-layer solution are generally slightly more accurate than those in the one-layer solution, and the working rate over all constituents is slightly closer to the Egbert and Ray numbers (Table 5). Note that

although we use the energy budget analysis of SHA, we do not employ mode-splitting, and consequently our energy inputs and outputs in the two-layer case balance much more closely (to 0.01 TW) than those in SHA.

Fig. 7 displays a map of the elevation discrepancies between our M_2 and K_2 solutions in the two-layer multi-constituent run and TPXO6.2. In both cases, the elevation difference is scaled by the globally averaged signal S of TPXO6.2, computed

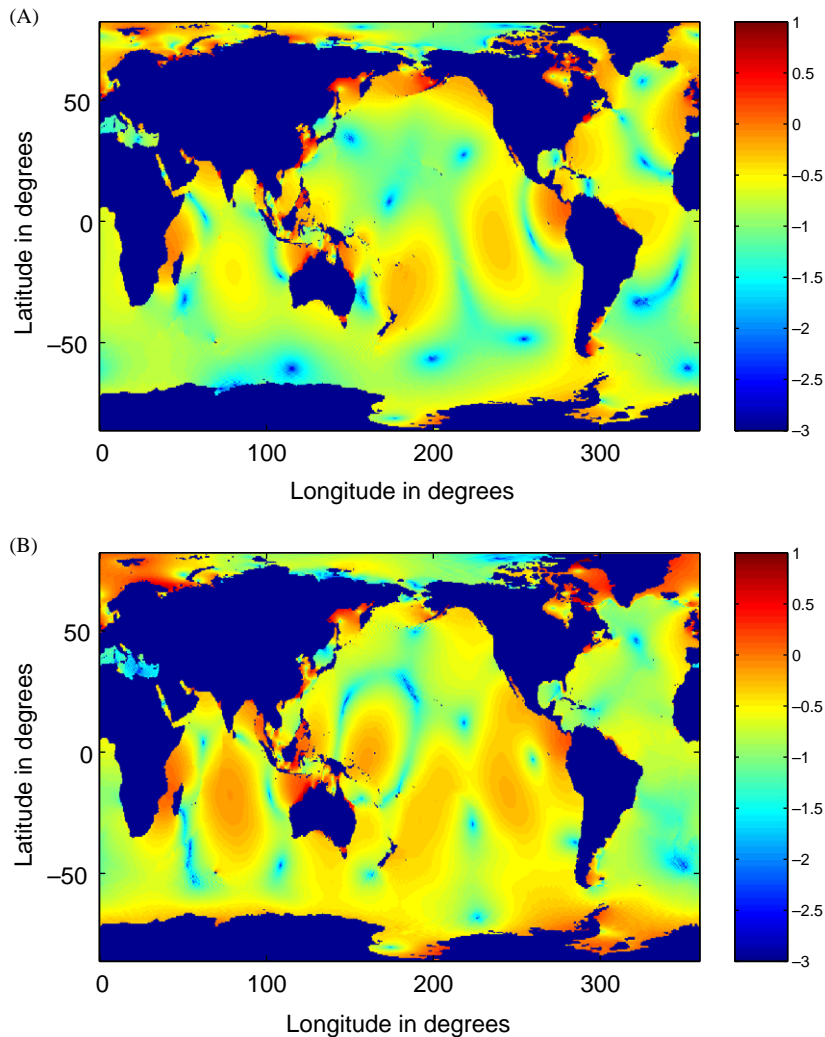


Fig. 7. (A) Log_{10} of normalized M_2 sea-level errors $\sqrt{\langle (\eta - \eta_{\text{TPXO6.2}})^2 \rangle} / S$ in the $1/2^\circ$ two-layer multi-constituent run, where brackets denote time-averaging, and S is the time- and area-averaged M_2 elevation signal of TPXO6.2 in waters deeper than 1000m and equatorward of 66° . (B) Same but for K_2 .

in waters deeper than 1000 m and equatorward of 66° . When unscaled (not shown) the M_2 map closely resembles the M_2 error map in the one-layer simulations, and is virtually indistinguishable, except at high latitudes, from an error map computed with respect to GOT99.2. The locations of large errors in the M_2 and K_2 maps are quite different. A frequency sensitivity in the appearance of error maps is also seen in Fig. 8, which plots the scaled elevation differences in the two-layer K_1 and O_1 solutions. In the diurnal maps “dimples”—the surface elevation signature of first mode baroclinic tides—can be seen between 30°S and

30°N , the latitudes of active diurnal internal tides. Correlations between the error maps for the various constituents were calculated. The highest correlation coefficients are between the S_2 and K_2 error maps (0.98), and the K_1 and P_1 error maps (0.97), consistent with the fact that these pairs lie close together in frequency. Coefficients for other diurnal pairs and semidiurnal pairs lie between 0.80 and 0.94. The frequency sensitivity of the error maps is reminiscent of the frequency sensitivity seen in the normal mode maps of Platzman et al. (1981). Correlation coefficients between maps of constituent errors and the

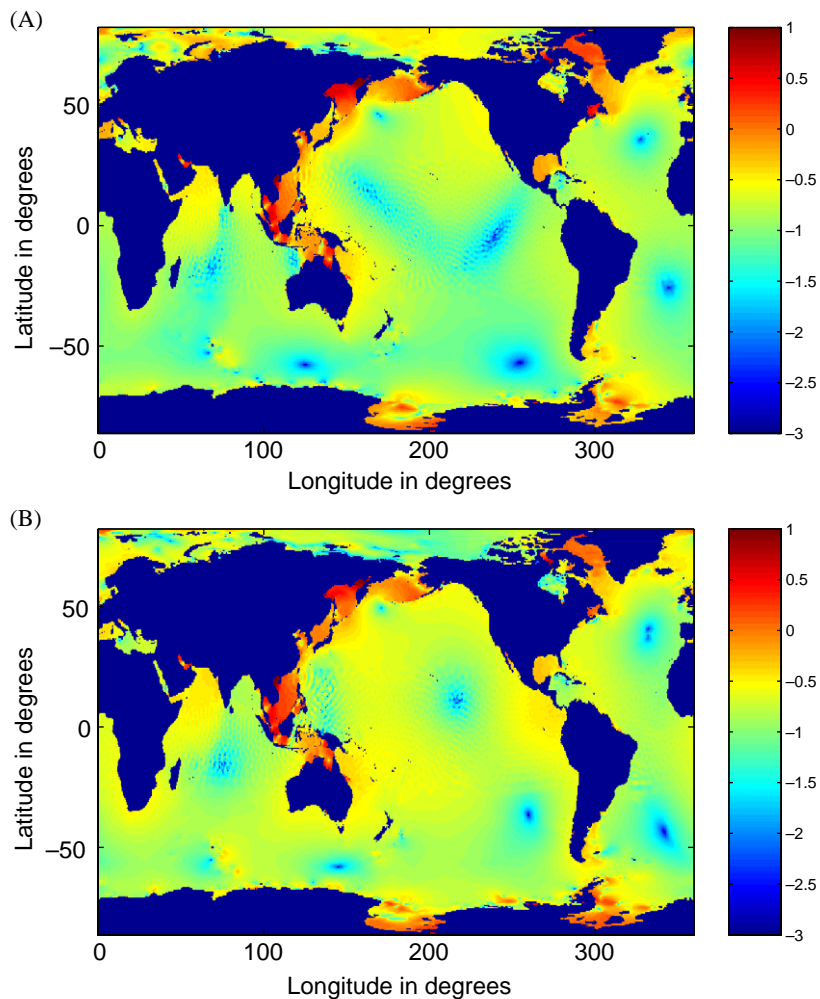


Fig. 8. As in the previous figure but for (A) K_1 and (B) O_1 .

corresponding constituent signals ranged from 0.76 to 0.88, indicating that large errors often occur where signals are large. Comparison of Fig. 8 with Fig. 9, which shows the K_1 and O_1 error maps in the one-layer multi-constituent run, indicates that baroclinicity alters the solution globally. Thus, the increase in accuracy seen in our two-layer K_1 solution in the Antarctic, which takes place despite the fact that our chosen g' values are more appropriate for mid-latitudes, may be due more to the greater accuracy of the solution elsewhere (which serves as a boundary forcing for southern latitudes) than to local effects.

Fig. 10 shows the amplitude and phase of K_1 surface elevations in our one-layer multi-constituent solution, in our two-layer multi-constituent solution, and in GOT99.2, along longitudes 140°E in the western Pacific and 330°E in the Atlantic, where relatively large reductions in the surface elevation errors are realized with baroclinicity (compare Figs. 8A and 9A). In the two-layer solution, the direct signature of the baroclinic tide is evident as small-amplitude, small-scale oscillations superimposed on the large-scale surface elevation fields. The inclusion of baroclinicity shifts the large-scale surface elevation field

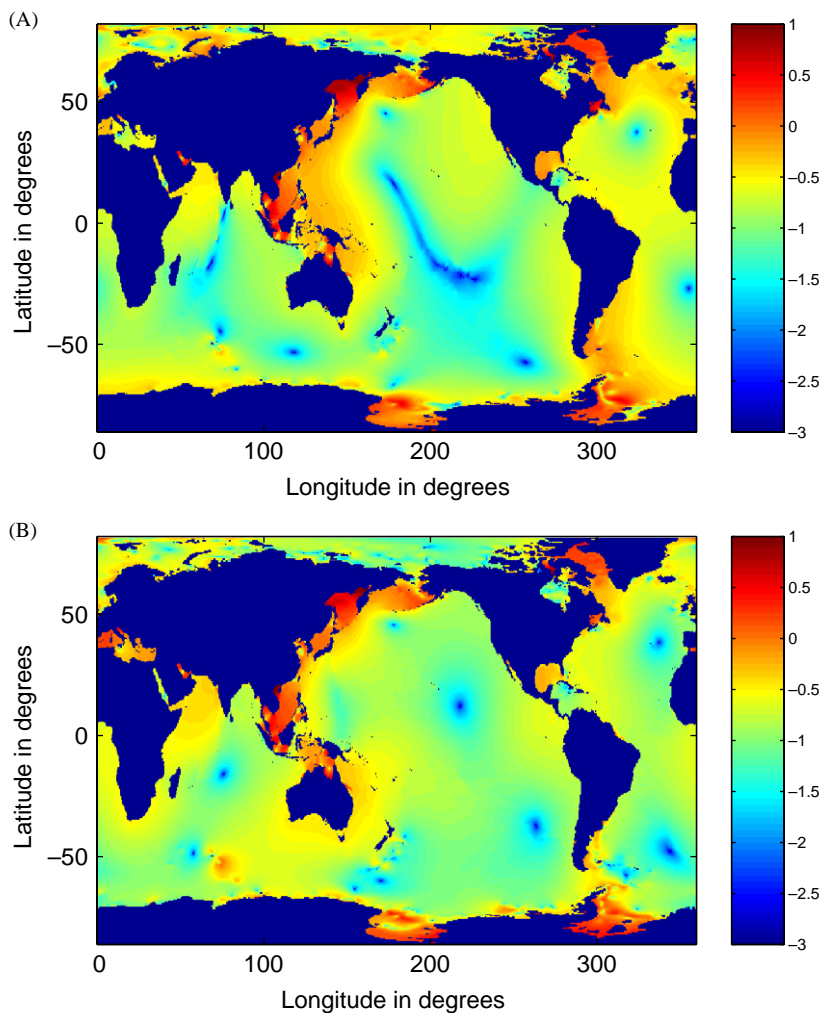


Fig. 9. As in the previous two figures but for (A) K_1 and (B) O_1 solutions in the $1/2^\circ$ one-layer multi-constituent run.

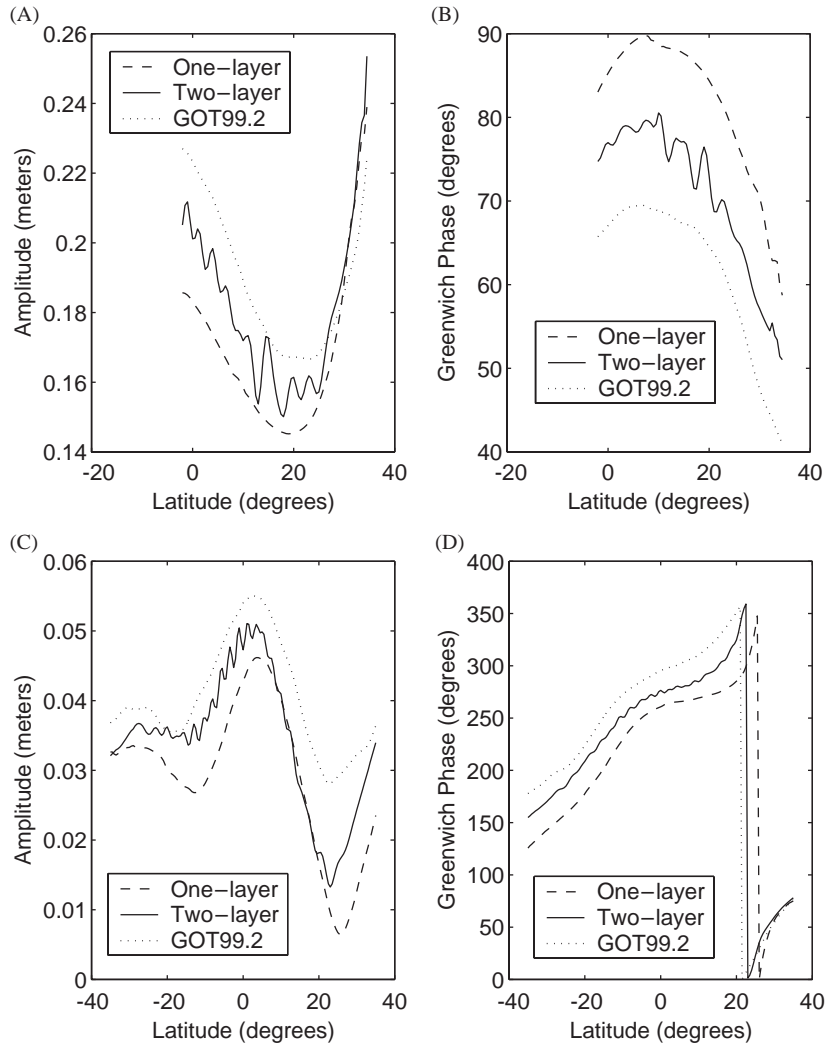


Fig. 10. Amplitude along (A) 140°E and (C) 330°E, and Greenwich phase along (B) 140° E and (D) 330° E of K_1 solutions.

towards the GOT99.2 elevations. It is this shift in the barotropic tide induced by baroclinicity, rather than direct surface effects, that lies behind the lower elevation errors in the two-layer run. Note that the baroclinic signature in the surface elevations is not evident in GOT99.2. As explained in Ray and Mitchum (1996, 1997), most T/P-constrained tide models filter out the baroclinic tide by averaging across tracks. Fig. 10 suggests that small spatial scales should perhaps be filtered out of the surface elevations in our two-layer model before comparison is made to elevations in

T/P-constrained models. However, we have chosen for simplicity not to perform such filtering, and we note that this choice is appropriate for comparison to pelagic tide gauge data, which does not filter out the surface signature of baroclinic tides.

6. Interfacial displacements and velocities in two-layer M_2 run

Fig. 11 displays a snapshot of the interfacial height in a $1/4^\circ$ two-layer M_2 -only experiment with

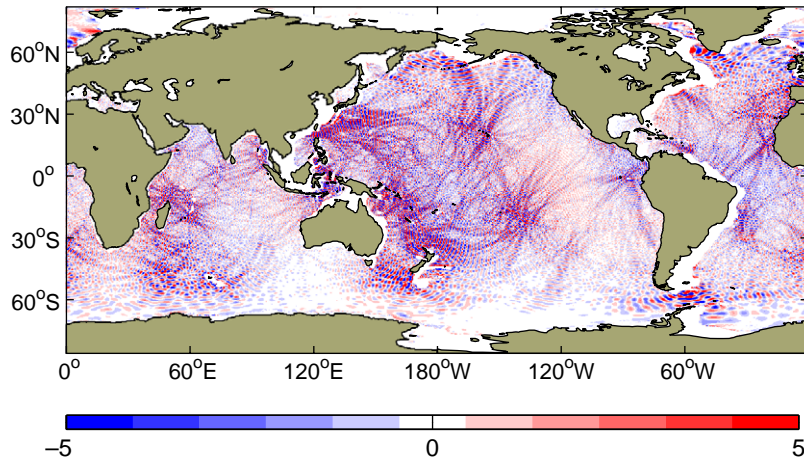


Fig. 11. Snapshot of interfacial height (m) in $1/4^\circ$ M_2 -only two-layer run with a multiplicative factor of 8, taken after the model has equilibrated. The lower layer only exists where the water column depth exceeds $700\text{-}\eta_2$ m.

a multiplicative factor of 8. The experiment has been iterated with respect to η_{SAL} . The snapshot was taken long after model equilibration was achieved. “Hotspots” for the generation of low-mode baroclinic tides, such as Hawaii, show up clearly. The globally integrated interfacial APE = $(1/2)\rho_0 \iint g'\eta_2^2 dA$ is 2.3 times lower than that of the two-layer nominal c_d -only experiment (i.e., the run without any topographic drag). The interfacial displacements in Fig. 8 of SHA are larger than those in our Fig. 11 (note the difference in scales), consistent with the lack of topographic drag in SHA. Topography was mapped onto the coarse model grids in different ways in the two papers, and that also may affect the interfacial displacements. Tidal beams do not appear to propagate as far from their sources in experiments with topographic drag as they do in experiments without topographic drag (again, compare Fig. 11 with Fig. 8 in SHA). Fig. 12 plots the spatial pattern of the ratio of modal kinetic energy densities $\langle (H_1 + H_2 + \eta_1)|\vec{u}_{\text{BC}}|^2 \rangle / \langle (H_1 + H_2 + \eta_1)|\vec{u}_{\text{BT}}|^2 \rangle$ in the $1/4^\circ$ M_2 -only run of Fig. 11. As in the interfacial displacement field, fine spatial structure is evident, with local values of the modal kinetic energy density ratio often being as large as 3. The ratio of temporally averaged global baroclinic to barotropic kinetic energy $\langle KE_{\text{BC}} \rangle / \langle KE_{\text{BT}} \rangle$ is 0.13; however, this ratio is sensitive to the amount of

horizontal friction present. A simulation with $K_H = 250\text{m}^2\text{s}^{-1}$ yielded a baroclinicity ratio of 0.20, while surface elevations were virtually unaffected. Fig. 13 plots the ratio of temporally averaged upper and lower layer squared speeds $\langle |\vec{u}_1|^2 \rangle / \langle |\vec{u}_2|^2 \rangle$ in the same $1/4^\circ$ M_2 -only run. Once again, much fine structure is evident, and local values of the ratio are often as high as ten. The larger tidal currents in the upper layer are likely due to the action of friction on the bottom layer as well as to the surface intensification of the baroclinic mode in the presence of thin thermoclines. Arbic and Flierl (2004) explores similar effects in idealized models of the mesoscale eddy field.

7. Summary and discussion

Over the last two decades, open-ocean tidal elevations have been mapped with high accuracy in models constrained by either tide-gauge or altimetric data. Some of these models are purely empirical, while others have hydrodynamical cores and assimilate data. Models of the latter type, for instance, Le Provost and Lyard (1997), have been able to accurately map tidal elevations without including substantial parameterized drag in the open-ocean parts of their domain. However, both

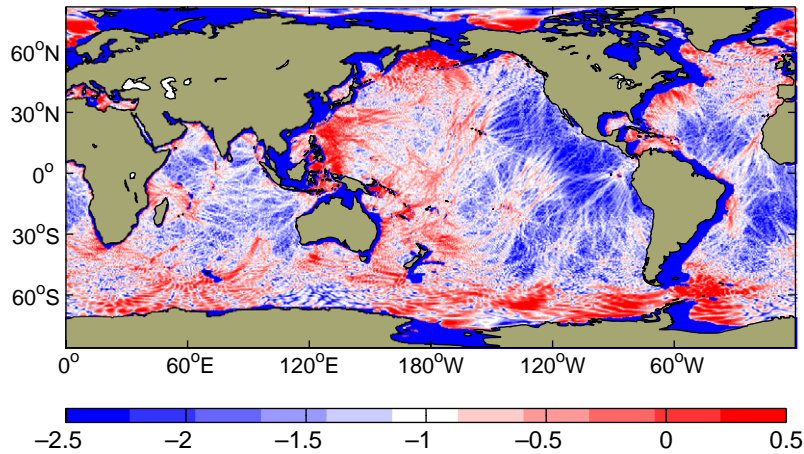


Fig. 12. Log_{10} of $\langle (H_1 + H_2 + \eta_1) |\bar{u}_{BC}|^2 \rangle / \langle (H_1 + H_2 + \eta_1) |\bar{u}_{BT}|^2 \rangle$, where brackets denote time-averaging, in the M_2 simulation of the previous figure. Areas with resting water column depths less than 700 m are shaded dark blue.

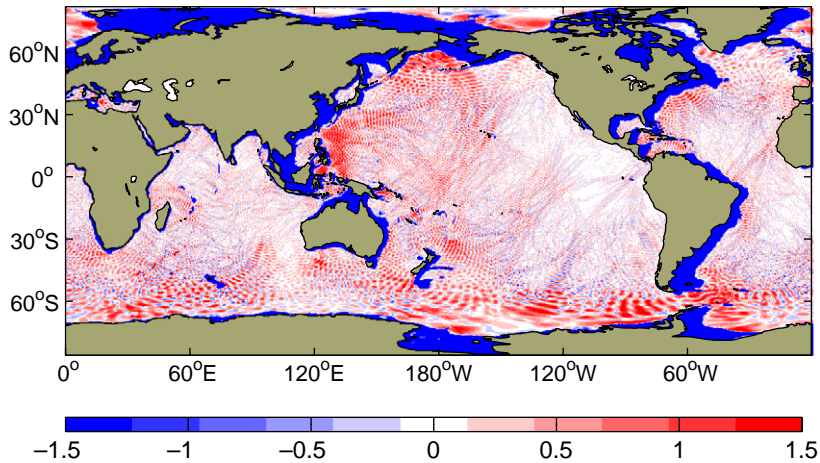


Fig. 13. Log_{10} of $\langle |\bar{u}_1|^2 \rangle / \langle |\bar{u}_2|^2 \rangle$, where brackets denote time averaging, in the M_2 simulation of the previous two figures. Areas with resting water column depths less than 700 m are shaded dark blue.

in situ observations and inferences from other T/P-constrained models suggest that substantial tidal dissipation (about 1 TW) takes place in the abyss. JS, CL, ERB, and the present paper have all found that the elevation accuracy of forward modeled tidal elevations is improved when substantial parameterized drag is included in the abyss. In this paper we have put forth a simple explanation for the sensitivity of model elevation accuracy to the parameterized drag. Both the APE and KE of

semidiurnal tides depend on the amount of abyssal drag. (The KE of both diurnal and long-period tides is sensitive to drag. The APE of diurnal tides is less sensitive to drag than is the APE of semidiurnal tides, and APE of long-period tides shows little sensitivity). Elevation errors are minimized when the model APE is near the observed value. Fairly accurate tidal elevations can be obtained in runs without topographic drag, in which other frictional parameters such as c_d or

K_H are treated as tunable, but only if c_d or K_H are made far larger than values that are physically plausible. Using topographic drag is preferable because it is physically motivated and concentrates the parameterized dissipation over areas of rough topography, as is seen in observations. Moreover, large K_H values would prohibit modeling of features which have small horizontal scales, such as coastal tides, baroclinic tides, and mesoscale eddies. Usage of topographic drag may open up the prospect for development of global models that capture both tides and the slowly varying oceanic general circulation with some degree of accuracy.

JS used the topographic drag formula $\rho_0 N k h^2 \bar{u} / 2$ for steady flow over monochromatic topography $h \sin(kx)$. They had no theoretical guidance behind their specific choices of h and k in the face of real topography, which has a spectrum of topographic heights and wavenumbers. Our scheme begins with an exact linear analysis for the drag on an oscillatory background flow over arbitrary small-amplitude topography. The linear analysis is supplemented by dimensional reasoning, based on arguments in the atmospheric literature, which differentiates between linear drag arising from radiating waves and quadratic drag arising from turbulence that results when flow deflects around topography. We have found that our calculated drag must be supplemented with a multiplicative factor, which we tune to minimize anomalies of our forward-modeled elevations against observations. Our current interpretation is that the multiplicative factor accounts for the unresolved small scales in the input topographic datasets, on which both flow-splitting and generation of breaking high mode internal waves likely take place. We find an optimal multiplicative factor of 7 in the one-layer M_2 -only case, and then use this factor across all constituents in one-layer multi-constituent simulations. It is the only free parameter in our model. JS also had a tunable parameter (topographic wavenumber k). The area-averaged decay rate in waters deeper than 1000 m lies between $(2.0 \text{ days})^{-1}$ and $(2.2 \text{ days})^{-1}$ in our optimally tuned run, the optimally tuned run in JS, and the optimally tuned run in Hirose et al. (2001), who examined the accuracy of models of

wind-driven barotropic motions. The consistency in decay rates suggests that topographic drag probably affects both wind-driven and tidal motions. Arbic and Flierl (2004) find that eddy vertical and horizontal structure in idealized models of baroclinically unstable geostrophic turbulence matches that of mid-ocean mesoscale eddies best when bottom friction is fairly strong. The current paper and others have argued that topographic drag may be a dominant source of this bottom friction.

Consistent with ERB, we have documented the lack of convergence in straightforward iterations of the self-attraction and loading term, and demonstrated that convergence can be achieved when a memory of the tidal elevations in prior iterations is retained. We have therefore obtained self-consistent forward solutions for the global tide. In waters deeper than 1000 m and in latitudes covered by the T/P altimeter, the sea-surface height discrepancy D against GOT99.2 in our optimally tuned ten-constituent one-layer forward model is 9.54 cm, slightly lower than the 10.1 cm found in JS. Across different constituents, the absolute values of D vary widely, but the percent variance captured is consistently high (84 percent or greater). The discrepancies of our one-layer multi-constituent forward model against the set of 102 pelagic tide gauges used in Shum et al. (1997) is 11.14 cm, substantially larger than the error measured against GOT99.2. However, the tidal signals sampled by the gauges are larger than the globally averaged signals in altimeter-constrained models, such that the percent elevation variance captured by our one-layer forward model is similar whether tide gauges or T/P-constrained models are used as the benchmark.

As far as we know, this paper and SHA are the first to publish simulations of baroclinic tides on a global scale. Both papers display global snapshots of the interfacial displacements, which show a great deal of fine structure including tidal beams. Both papers also document a substantial impact of baroclinicity on the tidal velocity field. Here we have mapped the ratio of temporally averaged baroclinic to barotropic kinetic energy densities, local values of which are as high as 3, and the ratio of temporally averaged squared upper to lower

layer current speeds, local values of which are as high as 10. SHA calculate conversion rates of barotropic to baroclinic tidal energy. In the present paper we have shown that the addition of another layer improves the surface elevation accuracy of our forward model across all of the larger constituents, when each of three different benchmarks is used. The improvement in surface elevation accuracy is not due to the direct elevation signature of the baroclinic tide, which is small, but to shifts in the surface elevations induced by baroclinicity. The RSS sea-surface height discrepancy of our multi-constituent forward tide model against GOT99.2 reduces from 9.54 to 8.90 cm, and the discrepancy against pelagic tide gauges reduces from 11.14 to 10.36 cm. Improvements in elevation accuracy from the one-layer to two layer model are also seen in waters deeper than 1000 m and south of 66°S, where we consider the TPXO6.2 model to be our benchmark. Against all three benchmarks, especially the Antarctic one, the improvement in elevation accuracy with baroclinicity is most noticeable for the P_1 and K_1 constituents. Our two-layer model apparently captures 98 to 99 percent of the open southern ocean diurnal height variance. The multiplicative factor for topographic drag was re-tuned in the two-layer case and the optimal value is 8. This is nearly the same as the optimal factor in the one-layer case, against our initial expectations that the explicitly resolved generation of low modes would allow less parameterized drag. In a follow-up paper we will combine the low-mode conversion diagnostic of SHA with the topographic drag used in the current paper to more thoroughly explore the roles of parameterized drag and resolved low-mode conversion in baroclinic tide models. We will explore the possibility that direct removal of energy from the low-mode baroclinic tides via parametric subharmonic instability (MacKinnon and Winters, submitted 2004) or other mechanisms, might allow a reduction in the amount of parameterized topographic drag needed at the bottom.

Maps of elevation error reveal large regions over which our forward model differs substantially from data-constrained models. We believe there-

fore that our forward model is still missing some important physics. It is possible that the lack of other oceanic motions in our model degrades its accuracy. This, however, seems unlikely to us, since the largest elevation errors do not generally occur in regions of strong currents. Furthermore, as measured by percentage of sea-surface height variance captured, our forward-modeled diurnal tides are more accurate than our semi-diurnal tides, despite the fact that diurnal frequencies lie closer to those of other energetic oceanic currents. Desai et al. (1997) found that the remaining errors in empirical ocean tide models are due largely to the oceanic general circulation. However, these errors are much smaller than those in our forward model. The general circulation affects the global distribution of density, which in turn affects the internal tides. Here we have used a single value of reduced gravity, and a single value of the resting interfacial depth, to characterize stratification, but stratification in the actual ocean is more complicated. Usage of the simpler topographic drag scheme of JS, or of large c_d or K_H values, produces elevation accuracies comparable to those achieved with our topographic drag scheme. ERB tried three different topographic drag schemes in their forward model and found little effect on elevation accuracy. We therefore doubt that changes to the drag scheme will make a practical difference in the elevation accuracy. Improvements in the underlying topographic datasets might reduce errors in forward models. The globally averaged sea-surface height discrepancy in preliminary M_2 experiments with the IOC et al. (2003, "GEBCO") topographic dataset is larger than in experiments using the Coward dataset, which was constructed primarily from Smith and Sandwell (1997). Model sensitivity to the underlying bathymetry, along with the related sensitivities to grid resolution and to the types and widths of filters used to map topographic datasets onto model grids, will be explored in a future paper. Another potential improvement to our forward tide model would be to use load calculations from a solid-earth model that incorporates lateral inhomogeneities (Tom Jordan, Tony Dahlen, Jerry Mitrovica, and Konstantin Letychev, personal communication 2003).

Acknowledgements

BKA thanks Laurie Padman and an anonymous reviewer for very thorough and helpful reviews; Richard Ray, Anand Gnanadesikan, and Steve Griffies for also improving the manuscript with their comments; Chris Garrett for steering him towards tides as an interesting problem; Gary Egbert and Richard Ray for patiently answering many questions about tides and for providing several useful datasets; Steve Jayne for much helpful practical advice; Raffaele Ferrari, Myrl Hendershott, Larry Horowitz, Isaac Held, Chris Kerr, Jody Klymak, Jennifer MacKinnon, Jim McWilliams, Jonathan Nash, David Nolan, Jonas Nycander, Isidoro Orlanski, Rob Pinkel, Kurt Polzin, David Sandwell, Walter H.F. Smith, John Toole, Andrew Wittenberg, Carl Wunsch, and Bill Young for useful discussions; Jeff Durachta, Brian Gross, Amy Langenhorst, John Sheldon, Buz Taylor, Hans Vahlenkamp, and Tim Yeager for help with computer software and hardware issues; and the Princeton University/GFDL Visiting Scientist Program for financial support during the course of this research. Simulations were performed on the supercomputer cluster at GFDL.

Appendix. Details of topographic drag scheme

We begin with the linear analysis for oscillatory background flow, and then discuss the augmentations from the dimensional analysis for drag due to low-level breaking. We assume for simplicity that the background flow is characterized by a single frequency ω . For simplicity, in this paper we take ω to be that of M_2 in all of our simulations, including those with multiple constituents. For the linear analysis, we assume that $|\vec{u}||\vec{k}| \ll \omega$, also for simplicity. (The linear solution in the general case is given by Bell, 1975a). Let the Fourier amplitudes of the topography be $\hat{h}(\vec{k})$, where $\vec{k} = (k, l)$ is the horizontal wavenumber. Let $u_{\vec{k}} = \vec{u} \cdot \vec{k}/|\vec{k}|$ be the component of the background flow \vec{u} along the gradient of the terrain component having wavenumber \vec{k} . The linear boundary condition is

$$\widehat{W}(\vec{k}) = iu_{\vec{k}}|\vec{k}|\widehat{h}(\vec{k}), \quad (24)$$

where $\widehat{W}(\vec{k})$ is the Fourier transform of $W(x, y) = w(x, y, z = 0)$, the vertical velocity component at the bottom. We assume gradual vertical variations such that $d(|m|^{-1})/dz \ll 1$, where m is the vertical wavenumber, and also assume $m \gg |d\bar{\rho}/dz|/\bar{\rho}$, where $\bar{\rho}(z)$ is the vertical profile of density. By ignoring horizontal variations of the Brunt–Vaisala frequency N , neglecting vertical variations of $\bar{\rho}$, and considering hydrostatic scales $|\vec{k}| \ll m$, we can write the WKB approximation

$$\widehat{w}(\vec{k}, z) = \widehat{W}(\vec{k}) \exp\left(i \int_0^z m dz'\right), \quad (25)$$

(e.g., Chapter 9 of Holton, 1972). For the oscillatory case

$$m = -N|\vec{k}|/\sqrt{\omega^2 - f^2}. \quad (26)$$

We have excluded nonhydrostatic waves by assuming that $\omega \ll N$. Note that throughout the analysis N refers to the value of N at the bottom, which we compute at every model gridpoint from Levitus et al. (1998).

From (24) and (25) it follows that, at the bottom,

$$\frac{\partial \widehat{w}}{\partial z} = \left(\frac{N|\vec{k}|}{\sqrt{\omega^2 - f^2}} \widehat{h}\vec{k} \right) \cdot \vec{u}. \quad (27)$$

Conservation of mass implies that $\partial w/\partial z = -\nabla \cdot \vec{u}'$, where \vec{u}' is a perturbation velocity, and since the momentum equation implies

$$\left(\frac{\partial^2}{\partial t^2} + f^2 \right) (-\nabla \cdot \vec{u}') = \bar{\rho}^{-1} \frac{\partial}{\partial t} \nabla^2 p', \quad (28)$$

where p' is a perturbation pressure, we may operate on (27) with the transform equivalent of $\bar{\rho} \nabla^{-2} (\partial^2/\partial t^2 + f^2)$ to obtain $\hat{p} = \bar{\rho} (N_* \hat{h} |\vec{k}|^{-1} i\vec{k}) \cdot \vec{u}$, where $N_* = N \sqrt{\omega^2 - f^2}/\omega$. If $\omega > |f|$, the Fourier synthesis is

$$p' = -\bar{\rho} \nabla \chi \cdot \vec{u}, \quad (29)$$

where χ is defined by

$$\chi(x, y) = -N_* \iint \frac{\hat{h}(\vec{k})}{|\vec{k}|} \exp(i\vec{k} \cdot \vec{x}) dk dl, \quad (30)$$

with $\vec{x} = (x, y)$. The spatial-transform equivalent is

$$\chi(x, y) = -\frac{N_*}{2\pi} \iint \frac{h(\vec{x}')}{|\vec{x} - \vec{x}'|} dx' dy', \quad (31)$$

which is a slightly smoothed version of the terrain $h(\vec{x})$. The input topography must be filtered to retain only the topographic scales that force internal gravity waves.

The drag is determined by the pressure at the bottom according to

$$\tau = -p' \nabla h = [\bar{\rho} \nabla \chi (\nabla h)^T] \vec{u}, \quad (32)$$

where the T superscript denotes the transpose operator. Formula (32), when multiplied by \vec{u} and averaged over one tidal cycle, is equivalent to the modal energy conversion formulae in Nycander (2004, submitted), except that Nycander uses a filter to limit the length scales over which (31) is computed, instead of imposing a sharp cutoff at 40 km as we did. The factor in brackets, which we denote by \bar{T} , is a tensor that depends only on the amplitude, variance, and anisotropy of the topography. In the Appendix we let angle brackets denote a grid-cell average and we obtain

$$\langle \tau \rangle = \langle \bar{T} \rangle \vec{u} \quad (33)$$

for the estimate of drag at the coarse resolution model gridpoints. The velocity perturbation becomes unbounded (resonant) at the latitudes where $\omega = |f|$, but the drag itself vanishes smoothly as these latitudes are approached from the equator. We set the drag to zero poleward of the latitude where f equals the M_2 frequency.

Over length scales small enough for the background flow to appear steady ($\omega \ll |\vec{u}| |\vec{k}|$) the nonlinearity parameter is the ratio of perturbation to background velocities $|\vec{u}'|/|\vec{u}|$, i.e., the Froude number

$$Fr = \frac{Nh}{|\vec{u}|}. \quad (34)$$

In the limit $\omega \gg |\vec{k}| |\vec{u}|$, the nonlinearity parameter is the ratio of nonlinear advection to the time tendency term, i.e. $|\vec{k}| |\vec{u}'|/\omega$. If we estimate $|\vec{k}| |\vec{u}'|/\omega \approx \nabla \cdot \vec{u}'/\omega$ and use $\nabla \cdot \vec{u}' = \partial_w / \partial z$ with the latter given by (27), we obtain $Fr(|\vec{u}'| |\vec{k}|/\omega)^2$ as our estimate of nonlinearity on large scales. The suggestion therefore is that nonlinearities are small

on large scales. Flow splitting and nonlinear drag appear to be operating primarily when $|\vec{k}| \gg \omega/|\vec{u}|$, i.e., over topographic wavelengths less than about 400 m for M_2 .

We now discuss the dimensional reasoning employed to include “nonpropagating” drag due to deflected flow and turbulence at the bottoms of large mountains. The dimensional reasoning we employ uses the Froude number $Nh/|\vec{u}|$ for steady flow (i.e., flow at small scales) as the nonlinearity parameter. We assume that the topography is characterized by well-defined features that can be binned into height ranges. If the mountain height exceeds a critical value h_c , the flow is blocked or deflected below a level $z = h - h_c$. For terrain features with heights less than h_c , the drag is entirely linear and propagating. For features with heights greater than h_c the drag includes both a propagating and a nonpropagating contribution. Internal waves are launched by the upper part of the mountain (over a vertical length scale h_c). In order to relate the width L of the “radiating” part of the mountain to elevation above the base, we introduce a power law with exponent δ :

$$L(z) = L_{\text{base}} (1 - z/h)^\delta, \quad (35)$$

where L_{base} is the width of the mountain base. We take $\delta = 1$ in the utilization of our scheme, which corresponds to an assumption that mountains are triangular, but we note that our drag scheme is not overly sensitive to this parameter.

For radiating linear waves, the drag can be scaled as $\rho N V h^2/L$, where V is the magnitude of the background velocity and L is the mountain length scale. The scaling for nonpropagating drag is $\rho V^2 (h - h_c)/L$. We set the nondimensional critical mountain height (or critical Froude number) $Fr_c = h_c(N/V)$.

The combination of these arguments is

$$\begin{aligned} D_p &= a_0 \min(1, (Fr_c/Fr)^{2-\delta}) Fr^2 (\bar{\rho} V^3 / NL_{\text{base}}), \\ D_{\text{np}} &= a_1 (1 - \min(1, (Fr_c/Fr_0)^{1+\delta})) \\ &\quad \times \frac{Fr_0}{1 + \delta} (\bar{\rho} V^3 / NL_{\text{base}}), \end{aligned} \quad (36)$$

where D_p and D_{np} refer to the propagating and nonpropagating parts of the base flux, respectively, and a_0 and a_1 are constant drag coefficients.

To evaluate (36) over the mountains contained by a gridpoint in the coarse resolution model, we must have a relationship between h and L_{base} . We assume that

$$L/L_0 = (h/h_0)^\gamma, \quad (37)$$

where L_0 , h_0 , and γ are constants (we denote the Froude number corresponding to h_0 by Fr_0). We determine the latter empirically to be about 0.35, but again, our model is not overly sensitive to this parameter.

Integrating (36) under the stated assumptions about mountain height distributions yields

$$\langle D_p \rangle = a_0 Fr_0^\gamma \frac{H^{<}(2 + \gamma) + H^{>}(\gamma - \delta) Fr_c^{2+\delta} \bar{\rho} V^3}{H(2\gamma) NL_0},$$

$$\langle D_{np} \rangle = a_1 Fr_0^\gamma \frac{H^{>}(1 + \gamma) - H^{>}(\gamma - \delta) Fr_c^{1+\delta}}{(1 + \delta)H(2\gamma)} \times \frac{\bar{\rho} V^3}{NL_0}, \quad (38)$$

where brackets denote spatial averaging, $H(\alpha) = [Fr_{\text{max}}^\alpha - Fr_{\text{min}}^\alpha]/\alpha$, and the superscript on H means that Fr is replaced with either $Fr^{<} = \min(Fr, Fr_c)$ or $Fr^{>} = \max(Fr, Fr_c)$. The minimum and maximum values of the Froude number over the unresolved topography (denoted by subscripts) serve as limits of the area integration. If we let $Fr \rightarrow 0$ in $\langle D_p \rangle$ we obtain

$$D^* = a_0 \bar{\rho} N V \Omega^2 / L_0,$$

$$\Omega = Fr_0^{\gamma/2} \frac{V}{N} \left[\frac{H(2 + \gamma)}{H(2\gamma)} \right]^{1/2}. \quad (39)$$

Refinements of the dimensional analyses above are presented in Garner (2004, submitted).

We allow the linear result (33) to determine the direction of drag, and modify our drag estimate by the dimensional analysis as

$$\langle \tau \rangle = \left(\frac{\langle D_p \rangle}{D^*} + \frac{\langle D_{np} \rangle}{D^*} \right) \tau^*, \quad (40)$$

where τ now refers to the final, corrected drag, and τ^* refers to the original linear result (33). The ratio of nonlinear to linear drag coefficients a_1/a_0 remains undetermined, as does the critical mountain height Fr_c . In the current paper we set the

former to 10 and the latter to 1, consistent with optimal values determined in atmospheric simulations.

Even using the best currently available global topographic datasets, it is impossible to directly estimate topographic heights, and thus Froude numbers, at horizontal scales of 400 m or less. In order to take advantage of quantities such as χ that were calculated over resolved scales, we computed

$$Fr_{\text{proxy}} = Fr_{\text{largescale}} \varepsilon(\phi), \quad (41)$$

as a proxy for the Froude number, where

$$Fr_{\text{largescale}} = \frac{|\nabla^2 \chi_{\text{steady}}| L}{V}, \quad (42)$$

and

$$\varepsilon(\phi) = \frac{V\omega}{2L(\omega^2 - f^2)}. \quad (43)$$

The quantity $Fr_{\text{largescale}}$ scales like a Froude number Nh/V . The extrapolation factor $\varepsilon(\phi)$ accounts for the reduction in topographic heights from those associated with resolved topographic scales to those associated with the unresolved horizontal length scales of interest. A typical tidal velocity is denoted by V , while L denotes a typical horizontal scale in the topography. The factor $\omega/(\omega^2 - f^2)$ is introduced into $\varepsilon(\phi)$ in order to make the Froude number large as ω approaches f , so that most of the drag is nonlinear at the resonant latitudes for the tides. As in the linear analysis, we use the M_2 frequency to calculate the Froude numbers. Since we are interested in Froude numbers for the small-scale (steady) limit, the quantity χ_{steady} must be used, where χ_{steady} is the equivalent of χ in the steady flow case— χ_{steady} is calculated as in (31) but with N_* replaced by N (Garner, 2003; and submitted 2004). Maps of Fr_{proxy} (not shown) indicate that it is of order one in areas of rough topography, and we used it in the dimensional analysis as if it was the Froude number calculated on the small scales where flow-splitting takes place. In the future we may consider whether more reliable estimates of the Froude number at small scales can be made. Perhaps the extrapolation from large to small scales could utilize (37). With $a_1/a_0 = 10$, $(\langle D_p \rangle +$

$\langle D_{np} \rangle / D^*$ does not vary by more than a factor of two over all Froude numbers. Thus alterations of the Froude number cannot change the drag by more than a factor of two. Such factors would be absorbed into our multiplicative factor.

References

- Accad, Y., Pekeris, C.L., 1978. Solution of the tidal equations for the M_2 and S_2 tides in the world oceans from a knowledge of the tidal potential alone. *Philosophical Transactions of the Royal Society of London* A290, 235–266.
- Andersen, O.B., Woodworth, P.L., Flather, R.A., 1995. Intercomparison of recent ocean tide models. *Journal of Geophysical Research* 100, 25261–25282.
- Arbic, B.K., Flierl, G.R., 2004. Baroclinically unstable geostrophic turbulence in the limits of strong and weak bottom Ekman friction: application to mid-ocean eddies. *Journal of Physical Oceanography* 34, 2257–2273.
- Armi, L., 1978. Some evidence for boundary mixing in the deep sea. *Journal of Geophysical Research* 83, 1971–1979.
- Baines, P.G., 1973. The generation of internal tides by flat-bump topography. *Deep-Sea Research* 20, 179–205.
- Baines, P.G., 1982. On internal tide generation models. *Deep-Sea Research* 29, 307–338.
- Balmforth, N.J., Ierley, G.R., Young, W.R., 2002. Tidal conversion by subcritical topography. *Journal of Physical Oceanography* 32, 2900–2914.
- Bell, T.H., 1975a. Lee waves in stratified flows with simple harmonic time dependence. *Journal of Fluid Mechanics* 67, 705–722.
- Bell, T.H., 1975b. Topographically generated internal waves in the open ocean. *Journal of Geophysical Research* 80, 320–327.
- Carrere, L., Lyard, F., 2003. Modeling the barotropic response of the global ocean to atmospheric wind and pressure forcing—comparisons with observations. *Geophysical Research Letters* 30, 1275 doi:10.1029/2002GL016473.
- Cartwright, D.E., 1977. Oceanic tides. *Reports on Progress in Physics* 40, 665–708.
- Cartwright, D.E., 1993. Theory of ocean tides with application to altimetry. In: Rummel, R., Sanso (Eds.), *Satellite Altimetry in Geodesy and Oceanography*. Springer, New York, pp. 99–141.
- Cartwright, D.E., 1999. *Tides: A Scientific History*. Cambridge University Press, Cambridge, p. 292.
- Cartwright, D.E., Edden, A.C., 1973. Corrected tables of tidal harmonics. *Geophysical Journal of the Royal Astronomical Society* 33, 253–264.
- Cartwright, D.E., Ray, R.D., 1990. Oceanic tides from Geosat altimetry. *Journal of Geophysical Research* 95, 3069–3090.
- Cartwright, D.E., Tayler, R.J., 1971. New computations of the tide-generating potential. *Geophysical Journal of the Royal Astronomical Society* 23, 45–74.
- Cox, C.S., Sandstrom, H., 1962. Coupling of surface and internal waves in water of variable depth. *Journal of the Oceanographic Society of Japan 20th Anniversary Volume*, 499–513.
- Cummins, P.F., Oey, L.Y., 1997. Simulation of barotropic and baroclinic tides off Northern British Columbia. *Journal of Physical Oceanography* 27, 762–781.
- Cummins, P.F., Cherniawski, Y., Foreman, M.G.G., 2001. North Pacific internal tides from the Aleutian Ridge: altimeter observations and modeling. *Journal of Marine Research* 59, 167–191.
- Desai, S., Wahr, J.M., 1995. Empirical ocean tide models estimated from TOPEX/POSEIDON altimetry. *Journal of Geophysical Research* 100, 25205–25228.
- Desai, S.D., Wahr, J.M., Chao, Y., 1997. Error analysis of empirical ocean tide models estimated from TOPEX/POSEIDON altimetry. *Journal of Geophysical Research* 102, 25157–25172.
- Doodson, A.T., 1921. Harmonic development of the tide-generating potential. *Proceedings of the Royal Society of London* A100, 305–329.
- Dushaw, B.D., Cornuelle, B.D., Worcester, P.F., Howe, B.M., Luther, D.S., 1995. Barotropic and baroclinic tides in the central North Pacific Ocean determined from long-range reciprocal acoustic transmissions. *Journal of Physical Oceanography* 25, 631–647.
- Egbert, G.D., Erofeeva, S.Y., 2002. Efficient inverse modeling of barotropic ocean tides. *Journal of Atmospheric and Oceanic Technology* 19, 183–204.
- Egbert, G.D., Ray, R.D., 2000. Significant dissipation of tidal energy in the deep ocean inferred from satellite altimeter data. *Nature* 405, 775–778.
- Egbert, G.D., Ray, R.D., 2001. Estimates of M_2 tidal energy dissipation from TOPEX/Poseidon altimeter data. *Journal of Geophysical Research* 106, 22475–22502.
- Egbert, R.D., Ray, R.D., 2003a. Semi-diurnal and diurnal tidal dissipation from TOPEX/Poseidon altimetry. *Geophysical Research Letters* 30, 1907 doi:10.1029/2003GL017676.
- Egbert, G.D., Ray, R.D., 2003b. Deviation of long-period tides from equilibrium: kinematics and geostrophy. *Journal of Physical Oceanography* 33, 822–840.
- Egbert, G.D., Bennett, A.F., Foreman, M.G.G., 1994. TOPEX/POSEIDON tides estimated using a global inverse model. *Journal of Geophysical Research* 99, 24821–24852.
- Egbert, G.D., Ray, R.D., Bills, B.G., 2004. Numerical modeling of the global semidiurnal tide in the present day and in the last glacial maximum. *Journal of Geophysical Research* 109, C03003 doi:10.1029/2003JC001973.
- Farrell, W.E., 1972. Deformation of the earth by surface loads. *Reviews of Geophysics and Space Physics* 10, 761–797.
- Flierl, G.R., 1978. Models of vertical structure and the calibration of two-layer models. *Dynamics of Atmospheres and Oceans* 2, 341–381.
- Foreman, M.G.G., 1977. *Manual for tidal heights analysis and prediction*. Pacific Marine Science Report 77-10, Institute of Ocean Sciences, 101pp.

- Francis, O., Mazzega, P., 1990. Global charts of ocean tide loading effects. *Journal of Geophysical Research* 95, 11411–11424.
- Garner, S.T., 2003. A topographic drag closure with analytical base flux. Paper P3.1, 14th Conference on Atmospheric and Oceanic Fluid Dynamics, American Meteorological Society.
- Gordeev, R.G., Kagan, B.A., Polyakov, E.V., 1977. The effects of loading and self-attraction on global ocean tides: the model and the results of a numerical experiment. *Journal of Physical Oceanography* 7, 161–170.
- Hallberg, R., Rhines, P., 1996. Buoyancy-driven circulation in an ocean basin with isopycnals intersecting the sloping boundary. *Journal of Physical Oceanography* 26, 914–940.
- Hendershott, M.C., 1972. The effects of solid earth deformation on global ocean tides. *Geophysical Journal of the Royal Astronomical Society* 29, 389–402.
- Hendershott, M.C., 1977. Numerical modeling of ocean tides. In: Goldberg, E.D., McCave, I.N., O'Brien, J.J., Steele, J.H. (Eds.), *The Sea*, vol. 6. Wiley, New York, pp. 47–95.
- Hendershott, M.C., 1981. Long waves and ocean tides. In: Warren, B.A., Wunsch, C. (Eds.), *Evolution of Physical Oceanography*. MIT Press, Cambridge, pp. 292–341.
- Hendry, R.M., 1977. Observations of the semidiurnal internal tide in the western North Atlantic Ocean. *Philosophical Transactions of the Royal Society of London* A286, 1–24.
- Hibiya, T., 1986. Generation mechanism of internal waves by tidal flow over a sill. *Journal of Geophysical Research* 91, 7696–7708.
- Hirose, N., Fukimori, I., Zlotnicki, V., Ponte, R.M., 2001. Modeling the high-frequency barotropic response of the ocean to atmospheric disturbances: sensitivity to forcing, topography, and friction. *Journal of Geophysical Research* 106, 30987–30995.
- Holloway, P.E., 1996. A numerical model of internal tides with application to the Australia North West Shelf. *Journal of Physical Oceanography* 26, 21–37.
- Holloway, P.E., Merrifield, M.A., 1999. Internal tide generation by seamounts, ridges, and islands. *Journal of Geophysical Research* 104, 25937–25951.
- Holton, J.R., 1972. *An Introduction to Dynamic Meteorology*. Academic Press, New York, 319pp.
- IOC, IHO, BODC, 2003. Centenary edition of the GEBCO digital atlas. Published on CD-ROM on behalf of the Intergovernmental Oceanographic Commission and the International Hydrographic Organization as part of the General Bathymetric Chart of the Oceans, British Oceanographic Data Centre, Liverpool.
- Jakobssen, M., Chervis, N.Z., Woodward, J., Macnab, R., Coakley, B., 2000. New grid of Arctic bathymetry aids scientists and mapmakers. *Eos Transactions, American Geophysical Union* 81, 89,93,96.
- Jayne, S.R., St. Laurent, L.C., 2001. Parameterizing tidal dissipation over rough topography. *Geophysical Research Letters* 28, 811–814.
- Jeffreys, H., 1920. Tidal friction in shallow seas. *Philosophical Transactions of the Royal Society of London* A221, 239–264.
- Kagan, B.A., Sundermann, J., 1996. Dissipation of tidal energy, paleotides, and evolution of the Earth–Moon system. *Advances in Geophysics* 38, 179–266.
- Kang, S.K., Foreman, M.G.G., Crawford, W.R., Cherniawsky, J.Y., 2000. Numerical modeling of internal tide generation along the Hawaiian Ridge. *Journal of Physical Oceanography* 30, 1083–1098.
- Kantha, L.H., 1998. Tides: a modern perspective. *Marine Geodesy* 21, 275–298.
- Kantha, L.H., Tierney, C.G., 1997. Global baroclinic tides. *Progress in Oceanography* 40, 163–178.
- Khaliwala, S., 2003. Generation of internal tides in an ocean of finite depth: analytical and numerical calculations. *Deep-Sea Research I* 50, 3–21.
- Kunze, E., Toole, J.M., 1997. Tidally driven vorticity, diurnal shear, and turbulence atop Fieberling Seamount. *Journal of Physical Oceanography* 27, 2663–2693.
- Ledwell, J.R., Montgomery, E.T., Polzin, K.L., St. Laurent, L.C., Schmitt, R.W., Toole, J.M., 2000. Evidence for enhanced mixing over rough topography in the abyssal ocean. *Nature* 403, 179–182.
- Legg, S., 2004. Internal tides generated on a corrugated continental slope. Part I: Cross-slope barotropic forcing. *Journal of Physical Oceanography* 34, 156–173.
- Le Provost, C., Lyard, F., 1997. Energetics of the M_2 barotropic ocean tides: an estimate of bottom friction dissipation from a hydrodynamic model. *Progress in Oceanography* 40, 37–52.
- Le Provost, C., Genco, M.L., Lyard, F., Vincent, P., Canceil, P., 1994. Spectroscopy of the world ocean tides from a finite element hydrodynamic model. *Journal of Geophysical Research* 99, 24777–24797.
- Le Provost, C., Bennett, A.F., Cartwright, D.E., 1995. Ocean tides for and from TOPEX/POSEIDON. *Science* 267, 639–642.
- Levitus, S., Boyer, T.P., Conkright, M.E., O'Brien, T., Antonov, J., Stephens, C., Stathoplos, L., Johnson, D., Gelfeld, R., 1998. *World Ocean Database 1998*, vol. 1: Introduction. NOAA Atlas NESDIS 18, U.S. Government Printing Office, Washington, D.C., 346pp.
- Llewellyn Smith, S.G., Young, W.R., 2002. Conversion of the barotropic tide. *Journal of Physical Oceanography* 32, 1554–1566.
- Llewellyn Smith, S.G., Young, W.R., 2003. Tidal conversion at a very steep ridge. *Journal of Fluid Mechanics* 495, 175–191.
- Lott, F., Miller, M.J., 1997. A new subgrid-scale orographic drag parameterization: its formulation and testing. *Quarterly Journal of the Royal Meteorological Society* 123, 101–127.
- Lueck, R.G., Mudge, T.D., 1997. Topographically induced mixing around a shallow seamount. *Science* 276, 1831–1833.
- Maas, L.R., Doelman, A., 2002. Chaotic tides. *Journal of Physical Oceanography* 32, 870–890.
- Marchuk, G.I., Kagan, B.A., 1984. *Ocean Tides*. Pergamon Press, Oxford, 292pp.

- Merrifield, M.A., Holloway, P.E., Shaun Johnston, T.M., 2001. The generation of internal tides at the Hawaiian Ridge. *Geophysical Research Letters* 28, 559–562.
- Miller, G.R., 1966. The flux of tidal energy out of the deep ocean. *Journal of Geophysical Research* 71, 2485–2489.
- Miranda, M.A., James, I.N., 1992. Non-linear three-dimensional effects on gravity-wave drag: splitting flow and breaking waves. *Quarterly Journal of the Royal Meteorological Society* 118, 1057–1081.
- Morozof, E.G., 1995. Semidiurnal internal wave global field. *Deep-Sea Research* 42, 135–148.
- Munk, W., 1997. Once again: once again—tidal friction. *Progress in Oceanography* 40, 7–35.
- Munk, W.H., MacDonald, G.J.F., 1960. *The Rotation of the Earth*. Cambridge University Press, London, 323pp.
- Munk, W., Wunsch, C., 1998. Abyssal recipes II: energetics of tidal and wind mixing. *Deep-Sea Research I* 45, 1977–2010.
- Niwa, Y., Hibiya, T., 2001. Numerical study of the spatial distribution of the M_2 internal tide in the Pacific Ocean. *Journal of Geophysical Research* 106, 22441–22449.
- Padman, L., Erofeeva, S., 2004. A barotropic inverse tidal model for the Arctic Ocean. *Geophysical Research Letters* 31, L02303 doi:10.1029/2003GL019003.
- Padman, L., Fricker, H.A., Coleman, R., Howard, S., Erofeeva, S., 2002. A new tidal model for the Antarctic ice shelves and seas. *Annals of Glaciology* 34, 247–254.
- Padman, L., Erofeeva, S., Joughin, I., 2003. Tides of the Ross Sea and Ross Ice Shelf cavity. *Antarctic Science* 15, 31–40.
- Parke, M.E., Hendershott, M.C., 1980. M_2 , S_2 , K_1 models of the global ocean tide on an elastic earth. *Marine Geodesy* 3, 379–408.
- Pawlowicz, R., Beardsley, B., Lentz, S., 2002. Classical tidal harmonic analysis including error estimates in MATLAB using T-TIDE. *Computers and Geosciences* 28, 929–937.
- Pierrehumbert, R.T., 1987. An essay on the parameterization of orographic gravity wave drag. *Proceedings seminar/workshop on observations, theory and modeling of orographic effects*, vol. 1, Shinfield Park, Reading, UK, ECMWF, pp. 251–282.
- Platzman, G.W., Curtis, G.A., Hansen, K.S., Slater, R.D., 1981. Normal modes of the world ocean. Part II: Description of modes in the period range 8–80 h. *Journal of Physical Oceanography* 11, 579–603.
- Polzin, K., 2004. Idealized solutions for the energy balance of the finescale internal wave field. *Journal of Physical Oceanography* 34, 231–246.
- Polzin, K.L., Toole, J.M., Ledwell, J.R., Schmitt, R.W., 1997. Spatial variability of turbulent mixing in the abyssal ocean. *Science* 276, 93–96.
- Pugh, D.T., 1987. *Tides, Surges and Mean Sea-level: A Handbook for Scientists and Engineers*. Wiley, Chichester, 472pp.
- Ray, R.D., 1994. Tidal energy dissipation: observations from astronomy, geodesy, and oceanography. In: Majumdar, S., et al. (Eds.), *Pennsylvania Academy of Sciences*, Easton, PA, pp. 171–185.
- Ray, R.D., 1998. Ocean self-attraction and loading in numerical tidal models. *Marine Geodesy* 21, 181–192.
- Ray, R.D., 1999. A global ocean tide model from TOPEX/POSEIDON altimetry: GOT99.2. National Aeronautics and Space Administration Technical Memorandum, NASA/TM-1999-209478, 58pp.
- Ray, R.D., Mitchum, G.T., 1996. Surface manifestation of internal tides generated near Hawaii. *Geophysical Research Letters* 23, 2101–2104.
- Ray, R.D., Mitchum, G.T., 1997. Surface manifestation of internal tides in the deep ocean: observations from altimetry and tide gauges. *Progress in Oceanography* 40, 135–162.
- Roosbeek, F., 1996. RATGP95: a harmonic development of the tide-generating potential using an analytical method. *Geophysical Journal International* 126, 197–204.
- Rudnick, D.L., Boyd, T.J., Brainard, R.E., Carter, G.S., Egbert, G.D., Gregg, M.C., Holloway, P.E., Klymak, J.M., Kunze, E., Lee, C.M., Levine, M.D., Luther, D.S., Martin, J.P., Merrifield, M.A., Moum, J.N., Nash, J.D., Pinkel, R., Rainville, L., Sanford, T.B., 2003. From tides to mixing along the Hawaiian Ridge. *Science* 301, 355–357.
- Schwiderski, E.W., 1980. On charting global ocean tides. *Reviews of Geophysics and Space Physics* 18, 243–268.
- Shum, C.K., Woodworth, P.L., Andersen, O.B., Egbert, G.D., Francis, O., King, C., Klosko, S.M., Le Provost, C., Li, X., Molines, J.-M., Parke, M.E., Ray, R.D., Schlax, M.G., Stammer, D., Tierney, C.C., Vincent, P., Wunsch, C.I., 1997. Accuracy assessment of recent ocean tide models. *Journal of Geophysical Research* 102, 25173–25194.
- Simmons, H.L., Hallberg, R.W., Arbic, B.K., 2004. Internal wave generation in a global baroclinic tide model. *Deep-Sea Research II*, this issue [doi:10.1016/j.dsr2.2004.09.015].
- Sjoberg, B., Stigebrandt, A., 1992. Computations of the geographical distribution of the energy flux to mixing processes via internal tides and the associated vertical circulation in the ocean. *Deep-Sea Research* 39, 269–291.
- Smith, W.H.F., Sandwell, D.T., 1997. Global sea floor topography from satellite altimetry and ship depth soundings. *Science* 277, 1956–1962.
- St. Laurent, L.C., Garrett, C., 2002. The role of internal tides in mixing the deep ocean. *Journal of Physical Oceanography* 32, 2882–2899.
- St. Laurent, L.C., Stringer, S., Garrett, C., Perrault-Joncas, D., 2003. The generation of internal tides at abrupt topography. *Deep-Sea Research* 50, 987–1003.
- Taylor, G.I., 1919. Tidal friction in the Irish Sea. *Philosophical Transactions of the Royal Society of London A* 220, 1–93.
- Thurnherr, A.M., Richards, K.J., 2001. Hydrography and high-temperature heat flux of the Rainbow hydrothermal site (36°14'N, Mid-Atlantic Ridge). *Journal of Geophysical Research* 106, 9411–9426.
- Thurnherr, A.M., Speer, K.G., 2003. Boundary mixing and topographic blocking on the Mid-Atlantic Ridge in the

- South Atlantic. *Journal of Physical Oceanography* 33, 848–862.
- Thurnherr, A.M., Richards, K.J., German, C.R., Lane-Serff, G.F., Speer, K.G., 2002. Flow and mixing in the rift valley of the Mid-Atlantic Ridge. *Journal of Physical Oceanography* 32, 1763–1778.
- Tierney, C.G., Kantha, L.H., Born, G.H., 2000. Shallow and deep water global ocean tides from altimetry and numerical modeling. *Journal of Geophysical Research* 105, 11259–11277.
- Wahr, J.M., 1981. Body tides on an elliptical, rotating, elastic and oceanless Earth. *Geophysical Journal of the Royal Astronomical Society* 64, 677–703.
- Wahr, J.M., Sasao, T., 1981. A diurnal resonance in the ocean tide and in the Earth's load response due to the resonant free "core nutation". *Geophysical Journal of the Royal Astronomical Society* 64, 747–765.
- Wunsch, C., 1975. Internal tides in the ocean. *Reviews of Geophysics and Space Physics* 13, 167–182.